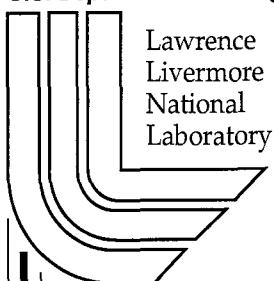


High Pressure, Solid State Experiments for NIF

B. Remington, J. Belak, J. Colvin, J. Edwards, D. Kalantar, B. Lasinski, S. Pollaine, H. Shay, S. Weber, B. Wolfer

February 15, 2001

U.S. Department of Energy



Lawrence
Livermore
National
Laboratory

DISCLAIMER

This document was prepared as an account of work sponsored by an agency of the United States Government. Neither the United States Government nor the University of California nor any of their employees, makes any warranty, express or implied, or assumes any legal liability or responsibility for the accuracy, completeness, or usefulness of any information, apparatus, product, or process disclosed, or represents that its use would not infringe privately owned rights. Reference herein to any specific commercial product, process, or service by trade name, trademark, manufacturer, or otherwise, does not necessarily constitute or imply its endorsement, recommendation, or favoring by the United States Government or the University of California. The views and opinions of authors expressed herein do not necessarily state or reflect those of the United States Government or the University of California, and shall not be used for advertising or product endorsement purposes.

This work was performed under the auspices of the U. S. Department of Energy by the University of California, Lawrence Livermore National Laboratory under Contract No. W-7405-Eng-48.

This report has been reproduced directly from the best available copy.

Available electronically at <http://www.doc.gov/bridge>

Available for a processing fee to U.S. Department of Energy
And its contractors in paper from
U.S. Department of Energy
Office of Scientific and Technical Information
P.O. Box 62
Oak Ridge, TN 37831-0062
Telephone: (865) 576-8401
Facsimile: (865) 576-5728
E-mail: reports@adonis.osti.gov

Available for the sale to the public from
U.S. Department of Commerce
National Technical Information Service
5285 Port Royal Road
Springfield, VA 22161
Telephone: (800) 553-6847
Facsimile: (703) 605-6900
E-mail: orders@ntis.fedworld.gov
Online ordering: <http://www.ntis.gov/ordering.htm>

OR

Lawrence Livermore National Laboratory
Technical Information Department's Digital Library
<http://www.llnl.gov/tid/Library.html>

High-pressure, solid-state experiments for NIF

Bruce Remington, Jim Belak, Jeff Colvin, John Edwards, Dan Kalantar,
Barbara Lasinski, Steve Pollaine, Hank Shay, Steve Weber, Bill Wolfer

Feb. 15, 2001

In this report, we summarize our plan for using NIF for measuring solid-state deformation physics at very high pressures, $P \gg 1$ Mbar. There are several key uncertainties, the strength and phase being two of them. The deformation mechanisms at high pressure and high strain rate are also uncertain. The state, as well as strength, of a material that has first been melted, then dynamically refrozen by high-pressure compression is very uncertain. There is no single facility that can address all of these issues at all parameter regimes of interest. Rather, a coordinated plan involving multiple laboratories and universities and multiple facilities will ultimately be needed. We present here our first thoughts for the NIF component of this effort.

In Sec. I, we motivate the physics of this regime, and point out the uncertainties, then describe in Sec. II the development work that we have done over the last 5 years in this area. In Sec. III, we describe several NIF designs we have developed to probe solid-state deformation physics at very high pressures.

I. Deformation Physics at High Pressure

Deformation physics at high pressure and high strain rate is of great interest in the field of material dynamics, with entire textbooks written on the subject. [Me 94] Yet data at $P \gg 1$ Mbar is scant to nonexistent and theoretical uncertainties are large. In Fig. 1 (reproduced from Soderlind and Moriarty [So 98]), the results from first principles calculations using the full potential, linear muffin tin orbital (FP-LMTO) theory for Ta are shown, to illustrate the level of uncertainties. Ta is a good material for illustration since it is a widely used bcc metal for high pressure deformation studies. The two curves in Fig. 1a bound the strength of Ta only to within a factor of ~ 4 at 10 Mbar. The lower curve scales the ambient yield strength by the shear modulus. The upper curve calculates the ideal crystal strength, defined as the minimum stress required to shear the perfect bcc crystal into itself. The actual strength of Ta is thought to lie somewhere in between. [So 98]

In Fig. 1b (reproduced from [So 98]), the energy difference for Ta between fcc and bcc, as a function of the axial distortion ratio c/a , again using FP-LMTO. At 2.5 Mbar, the dominant minimum is at $c/a=1$, which corresponds to a bcc configuration. At 10 Mbar, a secondary minimum starts to become apparent at $c/a = \sqrt{2}$, which corresponds to an fcc configuration. The fcc configuration is more densely packed than the bcc configuration, and it is suggested in [So 98] that at pressures above 10 Mbar Ta may undergo a transition to fcc. This transition is important, because bcc and fcc metals can behave differently in deformation. A bcc metal has a large Peierls barrier, deforms by transporting screw dislocations, and is prone to be in the thermal activation regime at low

temperatures. An fcc metal has a very low Peierls barrier, deforms by transporting edge dislocations, and is more likely to be in the phonon drag regime. Given these large uncertainties, experiments at $P \gg 1$ Mbar will be needed in the effort to develop a quantitative understanding of deformation physics at very high pressures.

Current experimental capabilities can readily access deformation physics at $P < \sim 1$ Mbar, as illustrated in Fig. 2. Examples are shown of diffraction measurements taken on a diamond anvil cell (Fig. 2a) at 500 kbar [Yo 95], diffraction on a powder gun shock experiment (Fig. 2b) at 20 kbar [Al 00], Rayleigh-Taylor (RT) measurements (Fig. 2c) on a high-explosion (HE) driven plate at ~ 100 kbar [Ba 74], spall on an imploded Al cylinder (Fig. 2d) at ~ 100 kbar [Ch 98], shock wave profiles on a gas gun (Fig. 2e) at ~ 100 kbar [Sw 89], and magnetically driven isentropic compression experiments (ICE) on Z in Fig. 2f. [As 99] At $P \gg 1$ Mbar, however, there are no current experimental capabilities for studying deformation physics in a well controlled, well diagnosed manner.

Deformation results from the generation and transport of dislocations, as illustrated in Fig. 3 (reproduced from [Hu 84]). A lattice responds to an applied shear stress by creating dislocations, that is, localized breaks in the lattice arrangement (Fig. 3a). These dislocations move across the lattice (Figs. 3b and 3c), and generate deformation when they break out the opposite side (Fig. 3d). Strength is the resistance of a material to deformation, which microscopically corresponds to the resistance to the transport of dislocations.

Deformation at a microscopic level is described by Orowan's equation,

$$d\epsilon/dt = \rho_m b v_d . \quad (1)$$

Here, ϵ is strain, ρ_m is mobile dislocation density, b is the Burger's vector (that is, the step size taken by a dislocation), and v_d is the dislocation average velocity. The different regimes of deformation can be illustrated by plotting dislocation velocity versus flow stress, as shown in Fig. 4a. The three regimes that we will be interested in are thermal activation, phonon drag, and shear wave limit.

In the thermal activation regime, dislocations spend most of their time, t_w , pinned against obstacles (for example the Peierls barrier in a bcc metal), waiting for a "thermal kick" over the barrier. Every so often a thermal fluctuation in the lattice assists the dislocation to get over the barrier, after which it quickly glides or "runs" in an interval of time t_r to the next obstacle a distance λ_2 away. The average dislocation velocity can then be written as

$$v_d = \lambda_2 / (t_w + t_r). \quad (2)$$

When the applied flow stress is large enough, a thermal kick is no longer needed for the dislocation to be above the barriers. In this regime, the resistance to dislocation motion is supplied by Newtonian drag, the source of which is phonon scattering. If the applied

flow stress is extremely high, the dislocation velocity is limited by another barrier, namely, the shear wave “speed limit”. Dislocations are thought to travel at speeds less than that of a shear wave (although theories of supersonic dislocations do exist).

These three regimes (thermal activation, phonon drag, shear-wave limit) can also be illustrated in a plot of flow stress vs strain rate, as shown in Fig. 4b. Specifically, what is plotted is the Steinberg-Lund constitutive model [St 89], given by

$$\dot{\epsilon} = \frac{1}{\frac{1}{C_1} \exp \left[\frac{F}{kT} \left(1 - \frac{Y_T}{Y_p} \right)^2 \right] + \frac{C_2}{Y_T}} \quad (3)$$

The input parameters C_1 , F , Y_p , and C_2 are physically based, as described originally by Hoge and Mukherjee [Ho 77], and scale with P , $\eta = \rho/\rho_0$, T , and ρ_m according to

$$C_1 = \rho_m b \lambda_2 v_e \sim \rho_m b^2 \sim \rho_m / \eta^{2/3}, \quad (4a)$$

$$C_2 = D/\rho_m b^2 \sim D\eta^{2/3}/\rho_m \sim \eta^{4/3} T^{1/2}/\rho_m, \quad (4b)$$

$$F \text{ (activation energy)} \sim b^3 G, \quad (4c)$$

$$Y_p \text{ (Peierls stress)} \sim G, \quad (4d)$$

and ρ_m (mobile dislocation density) is a function of strain and shock strength. Here b is the Burger’s vector, λ_2 is the distance between obstacles (λ_1 is the width of obstacles), and D is the phonon drag coefficient. The input parameters chosen for Fig. 4b were arbitrarily chosen to illustrate the different regimes of deformation. When Y_p (Peierls stress or barrier) is large compared to the applied shear stress (Y_T), the exponential term in the denominator of Eq. 3 dominates, and the deformation mechanism is thermal activation. When $Y_p < Y_T$, the exponential term is neglected, and the deformation is dominated by phonon drag. At low strain rate (ie, low applied shear stress) and temperature, thermal activation dominates, whereas at high strain rate and temperature, phonon drag is the dominant mechanism for resisting deformation. At the ultrahigh strain rates ($> \sim 10^8 \text{ s}^{-1}$), the shear wave speed sets an additional limit to dislocation transport. At strain rates greater than a few times 10^8 s^{-1} , a different mechanism such as twinning may be activated, but exactly how a material deforms at such high strain rates is very uncertain. [Me 94] A key question is whether deformation mechanism really does scale with strain rate and temperature, as just suggested. A need exists for high pressure, high strain rate experimental capabilities that can access both the thermal activation and the phonon drag regimes at a wide range of strain rate, to be able to test the models and simulations under relevant conditions. Ultrahigh strain rate deformation accesses a new regime of solid-state physics, which is of high visibility, and attractive to university collaborators.

Deformation physics is a complex multiscale problem. To break this down into manageable pieces, we decompose the deformation mechanisms into regimes by spatial scale, as illustrated in Fig. 5. [La 99] The smallest scale, the electronic scale, corresponds to the atomic structure of isolated or small groups of atoms. The next level up in size, the atomistic scale, corresponds to collections of, say, 10^6 atoms in a lattice array. The spatial scale in the atomistic regime is of order fractions of a micron on a side, and lattice dynamics is the deformation physics of interest. Here, shocked single-crystal diffraction experiments can probe the lattice dynamics. [Lo 01] The next level up, the microscale, corresponds to spatial scales of 10's of microns on a side. In this regime, the deformation physics of interest is dislocation dynamics. A traditional way of investigating this regime is by shock recovery experiments. Post-shot TEM characterization of shocked samples reveals the residual microstructure. [Me 01] The next step up in spatial scale is the mesoscale, which corresponds to collections of grains (as opposed to collections of atoms). Here, spatial scales are measured in fractions of millimeters. Rayleigh-Taylor experiments can show the effects of grains on the dynamics in this regime. [Co 01] Finally, at the largest scales, the material behaves as a continuum, and strong-shock experiments reside in this regime. [Bu 99, Re 01] The key to understanding deformation physics at a fundamental level is to develop theories and models suitable for each regime of spatial scale, and use simulations to connect the regimes. Here, laser experiments offer a powerful tool to test the models in the individual regimes, and test the simulations by experimentally connecting the regimes. The experimental techniques for each scale have already been demonstrated, as suggested by the experimental images below in Fig. 5. We next describe in more depth examples of experiments in each regime from our work on the Nova, Omega, and Trident lasers over the past 5 years.

II. Experimental Techniques

We start with the atomistic scale – collections of atoms at the lattice level (see Fig. 5). At this level, time resolved diffraction from single crystals is an excellent probe of the response of the lattice to a shock or shocks. In the illustration shown in Fig. 6a, a point source of x-rays impinges on a single crystal. In the “Bragg direction”, the lattice compression in the direction of shock propagation is probed. In the “Laue direction”, we probe the lattice response in the direction orthogonal to the shock propagation. An example of streaked shocked Si data in the Bragg direction is shown in Fig. 6b. These types of laser-based dynamic diffraction techniques have been under development over the past 15 years on the Trident, Janus, Vulcan, Nova, and Omega lasers [Wa 87; 89; 94; Wh 95; Wo 90; Wo 97] The diffraction techniques thus developed should be applicable on NIF. The work shown in Fig. 6 is from a LLNL-LANL-Oxford University collaboration, under the Science Use of Nova (SUN) and National Laser Users’ Facility (NLUF) Programs on the Nova and Omega lasers.

The analysis of a series of shocked Si and Cu diffraction experiments done on Nova and Omega is shown in Fig. 7. In the Bragg direction, the Si showed increased lattice compression as the strength of the shock was increased (Fig. 7a), but interestingly showed no lattice response in the orthogonal (Laue) direction (Fig. 7b). To the contrary, experiments on shocked single crystals of Cu at nominally the same shock strength

showed a prompt lattice response in both the Bragg (Fig. 7c) and Laue (Fig. 7d) directions. This difference in lattice response between Si and Cu reflects the difference in their Peierls barriers. Si, a covalently bonded material with a diamond crystal structure, has a very high Peierls barrier. Consequently, the dislocations (the carriers of plastic deformation) stay pinned against these obstacles, and the Si lattice cannot deform plastically on the 10 ns time scale of our experiments. The Si deforms uniaxially, like a 1D spring. (The two-wave pattern of compression observed in some of the experiments in the Bragg direction of Si is from two or more shocks being launched due to the time dependence of the radiation drive over its 3-4 ns duration.) The Peierls barrier of Cu, a fcc crystal, is lower by a factor of $\sim 10^3$ [Hu 84], dislocations easily jump over the barriers, and the Cu lattice promptly deforms plastically in a 3D compression. [Lo 01] Hence, this technique of multi-lattice diffraction to observe the characteristic time scale of 3D (plastic) lattice response appears capable of dynamically probing the Peierls barrier at high pressure, on nanosecond time scales, and in the presence of multiple shocks. This capability will be very useful in developing a microscopic understanding of deformation mechanisms, as the Peierls barrier (Y_p) is a key parameter in Eq. 3. When Y_p is small (relatively speaking), the deformation mechanism is likely to be phonon drag, whereas when Y_p is large, the mechanism is prone to be thermal activation (at low temperature).

Comparing the diffraction data with post-processed, molecular dynamics (MD) simulations shows great promise for understanding lattice dynamics in much more detail. An example MD simulation of a shocked Cu (fcc) lattice is shown in Fig. 8a. Behind the shock, there are bands of stacking faults. The lattice does not respond homogeneously to shock compression, but rather in localized bands of stacking faults. In these bands, the normal ABCABC stacking sequence for an fcc lattice switches to an ABABAB sequence characteristic of an hcp lattice. In between these bands, the fcc lattice is preserved, but in a 3D compressed state. The higher the density of stacking faults, the lower the predicted amplitude of the diffraction signal from the shocked crystal (Fig. 8b). These stacking fault bands cause slight phase mismatches in the fcc regions in between. This both broadens the shocked diffraction signal and can shift the location of its centroid (Fig. 8c). The results in Fig. 8c correspond to an MD simulation by Peter Lomdahl and Brad Holian at LANL, post-processed to produce a simulated Bragg diffraction signal by Andrew Loveridge-Smith and Justin Wark, at Oxford University. The shocked diffraction signal is predicted to be much lower, broader, and shifted in position. Many of these features are seen in our shocked Cu data, as shown in Fig. 8d. A more careful analysis and comparison with the MD simulations may allow stacking fault density and perhaps $\rho_{\text{dislocation}}$ to be inferred dynamically.

A traditional approach to investigating the deformation physics at the microscale is to shock samples, recover them, and use transmission electron microscopy (TEM) to examine the residual microstructure created. We illustrate the results of such a recovery experiment shocking mm-sized single crystals of Cu on the Omega laser in Fig. 9. The thick Cu single crystals were shocked at a range of pressures by direct illumination, and recovered in tubes filled with aerogel foam (Fig. 9a). The recovered samples (Fig. 9b) were sectioned and analyzed by TEM at UCSD by Marc Meyers and his group. The residual microstructure shows clear sensitivity to the strength of the shock, [Me 01] with

microstructure corresponding to dislocation cells, microtwins, and fully-formed twins being observed (Fig. 9c, 9d, 9e). (The pressures given in Fig. 9c-e are only order-of-magnitude estimates.) This project is a LLNL-UCSD collaboration, under the NLUF program.

To illustrate the techniques used at the next step-up in scale, we refer to the technique developed nearly 30 years ago by Barnes at LANL. Barnes used the Rayleigh-Taylor (RT) instability as his “detector” of solid-state strength. He “softened” the HE drive, by putting a gap between the HE and the Al payload (Fig. 10a). When the HE detonates, it expands and decompresses across this gap, and shocklessly accelerates a rippled Al foil. Barnes measured the RT growth by side-on radiography, examples of which are shown in Fig. 10b. He used the reduction from classical (ie, liquid) as a measure of strength. In simulations, he systematically increased the Al strength until the simulations reproduced his data (Fig. 10c), thereby estimating the strength of Al at 100 kbar. [Ba 74] Lebedev and Raevski at Sarov in Russia have extended Barnes original work to pressures of 700 kbar and with samples of Al and Ti. [Le 93, 96, 97]

To obtain higher pressures and access the mesoscale, we replaced the HE drive used by Barnes, Lebedev, and Raevski with the Nova laser, and used much smaller (“mesoscopic”) samples (Fig. 11a). This allowed us access to solid-state deformation physics at $P > 1$ Mbar. [Ka 00] We developed a shaped radiation drive on the Nova laser (Fig. 11b) to accelerate an RT unstable Al foil. By using staged shocks, we can keep the Al solid, but now at pressures of ~ 1 Mbar. The RT growth of preimposed sinusoidal ripples is measured by time-resolved, face-on radiography. An example inflight radiograph taken at $t = 20.5$ ns of a foil with side-by-side ripples of $\lambda_1 = 50 \mu\text{m}$ and $\lambda_2 = 20 \mu\text{m}$ wavelength is shown in Fig. 11c. The amplitude of the ripples can be inferred from the contrast in optical depth, δOD . Like Barnes, we use departures of the RT growth from classical (liquid) to infer the strength (Fig. 11d). Our pressures ($P \sim 1$ Mbar) and strain rates ($d\epsilon/dt \sim 10^8 \text{ s}^{-1}$) were high, and our tentative conclusion is that the strain-rate-independent Steinberg-Guinan (SG) model is, by itself, not adequate under these conditions. The SG model for yield stress is given by [St 81]

$$Y_{\text{SG}} = Y_0(1+\beta\epsilon^n)[aP/\eta^{1/3} + b(T-300)] , \quad (5)$$

where for 6061 Al, $Y_0 = 2.9 \times 10^{-3}$ Mbar, $\beta = 125.$, $n = 0.10$, $a = 6.52 \text{ Mbar}^{-1}$, $b = 6.16 \times 10^{-4} \text{ K}^{-1}$, and $\eta = \rho/\rho_0$.

A very interesting outcome from our experiment was the realization that the grain size could be inferred inflight. As the material flows from bubble to spike near the CH(Br)-Al interface, driven by the RT instability, there could be preferential slippage at the grain boundaries. This slippage serves as an added seed to the RT growth, and the overall perturbation becomes the superposition of the random 3D grain pattern (Fig. 12a) with the pre-imposed 2D sinusoidal ripples (Fig. 12b). By removing the ripples in the data analysis via a Fourier filter (Fig. 12c), we can deduce the inflight grain size distribution (Fig. 12d). The grain size distribution inferred from the $\lambda = 20 \mu\text{m}$ ripple side of the RT

foil agrees quite well with the grain distribution from the initial grain characterization. The agreement from the $\lambda = 50 \mu\text{m}$ side is not quite so good, which may be an indication of nonlinear mode-coupling effects. In further analysis, the instrument MTF, RT dispersion curve, and mode coupling would have to be taken into account. Nevertheless, this technique looks promising, and will be very useful as a measure of grain size in the refreeze experiments that we are designing for NIF.

Experiments to probe the continuum regime are possible on lasers, as well. By either using samples whose dimensions are much greater than the characteristic grain size, or driving the sample into the liquid state, so that there are no grain effects, the sample flows as a continuum medium. We show some examples of experiments that are in the continuum regime from Nova and Omega. In experiments where we drove a weak shock through thick ($200 \mu\text{m}$) Al, we can approximate this as being in the continuum regime, because in this case, the sample size was much larger than the grain size. We used VISAR to measure shock wave profiles for weak shocks, as shown in Fig. 13a. The classic elastic-plastic wave profile is evident in Fig. 13b. These type of weak shock wave profiles can be used to “dial in” the parameters of constitutive models, much like Steinberg did in his original paper [St 81]. However, this works only for weak shocks, $P \sim 100 \text{ kbar}$, or less. For $P > 1 \text{ Mbar}$, the plastic wave overruns the elastic wave, and there are no distinguishing features to fit other than a single strong shock front. We also use VISAR as our primary shock timing diagnostic. For the shaped drive that we will develop on NIF, having a reliable shock speed diagnostic via this VISAR technique will be crucial. We illustrate a VISAR measurement of shock transit through a stepped CH foil as an example of shock timing done on Omega (Fig. 13c).

At the continuum level, a standard diagnostic for complex hydrodynamic evolution is side-on radiography, an example of which is shown in Fig. 14. With very good spatial and temporal resolution, we can see great detail as the hydrodynamics evolves, even into the deep nonlinear regime. We show an example of a strongly shocked, planar, multilayer experiment done on the Omega laser. The target corresponds to layers of CH_2 , Cu, CH, CH(Br), and CRF foam, with a $\lambda = 200 \mu\text{m}$, $\eta_0 = 20 \mu\text{m}$ ripple at the Cu-CH interface. A strong shock, $P \gg 1 \text{ Mbar}$, was launched by direct illumination of the thin CH_2 ablator. At the rippled Cu-CH interface, there is an initial phase of Richtmyer-Meshkov instability growth followed by a protracted phase of RT growth, as the Cu is decelerated by the CH, triggering large RT spikes of Cu. Notice, we can observe all relevant details: Cu layer, CH layer, CH(Br) layer, shocked foam layer, unshocked foam layer, perturbation growth at the Cu-CH interface, and even an exquisite edge vortex. [Kane 01] This work is part of a LLNL-Univ. of Michigan -Univ. of Chicago -Univ. of Arizona collaboration, through the NLUF Program.

We show examples of an exploding cylindrical RT experiment [Bu 99, Re 01] done on Nova (Fig. 15a) and an imploding spherical RT experiment [Gl 00] in Fig. 15b. As can be seen, even complex imploding and exploding geometries can be well diagnosed. Hence, we will have great flexibility in designing and diagnosing experiments on NIF in planar, cylindrical, spherical, imploding, and exploding geometries. The physics goals and regimes will dictate the experimental configuration, and the diagnostic flexibility will

allow us to measure the physics and see what happens. The cylindrical explosion experiment was a collaboration between LLNL-LANL-SUNY Stony Brook, through the Science Use of Nova (SUN) Program. The spherical ICF implosion experiment was done as a LLNL-CEA collaboration.

This completes our discussion of the diagnostic techniques that will allow access to the deformation physics from the atomistic to the continuum scale. We next turn to our designs for experiments on NIF that will allow us to access the very high pressure regimes over a range of strain and strain rate.

III. NIF Designs

We have developed a total of 14 NIF designs to study metal deformation physics at very high pressure, where the theories and modeling are most uncertain. Our designs span nearly 2 orders of magnitude in pressure and strain rate, namely, pressures of 0.7-25 Mbar, and strain rates of $10^6 - 10^8 \text{ s}^{-1}$. Examples from 5 of these designs are presented in the following.

In our first NIF design (NIF experiment #1 in Fig. 26), we use direct illumination on a large cylinder (1 cm long by 0.5 cm diameter), which is imploded against 10 mg/cm^3 foam, as shown in Fig. 16a. The cylinder outer wall is a $25 \mu\text{m}$ CH ablator, and the inner wall is a $100 \mu\text{m}$ Ta payload. The laser intensity is assumed to be uniform at $1.25 \times 10^{13} \text{ W/cm}^2$ for 40 ns (Fig. 16b), assuming we stack two sets of 20 ns NIF beams. As the Ta cylinder implodes against the foam, it will decelerate, starting at $\sim 600 \text{ ns}$, at which time the Ta-foam interface will be RT unstable. By end-on radiography (similar to that shown in the cylindrical explosion image in Fig. 15a), we will be able to see preimposed perturbations growing, and thereby infer strength by departures from classical RT growth.

This high strain, low strain rate cylindrical experiment is designed to never melt during the times of interest. Shown in Fig. 17a is the Ta temperature (T_e), compared to the melt temperature (T_m) as calculated by the Lindemann melt law. The initial shock phase happens during the first 40 ns, followed by a coast phase from 40 ns to 500 ns. The compression-stagnation-deceleration phase occurs from 600-800 ns, where the pressures rise to a maximum of $\sim 2 \text{ Mbar}$ at peak strains of ~ 3 (see Fig. 17b) and characteristic strain rates of $\sim 3 \times 10^6 \text{ s}^{-1}$. The radial convergence of this design is $R_0/R_{\min} \sim 10$. We have a lower convergence (~ 5) design with similar strain rates but at lower peak pressure ($\sim 0.7 \text{ Mbar}$). The NIF laser scientists have confirmed that backlighting with delays as large as $1 \mu\text{s}$ is possible, which will be required for this experiment.

A more advanced design of this cylindrical implosion (NIF experiment #2 in Fig. 26), accesses strain-induced melt and high-pressure refreeze. The geometry of this more advanced design is similar to that shown in Fig. 16, but we now use a 3-step shaped drive, shown as total laser power vs. time in Fig. 18a, and as single-beam power vs. time in Fig. 18b. With this shaped drive, the Ta cylinder (1) stays solid during the initial

shock phase, (2) melts during the coast phase due to strain-induced viscous heating, (3) refreezes early in the compression phase (Fig. 18c), and (4) reaches peak pressures of ~ 10 Mbar during the deceleration-RT phase, as shown in Fig. 18d. Again, end-on, hard-x-ray radiography will be used to observe the RT growth during deceleration. Strength will be inferred by the reduction of RT growth compared to classical (liquid). Note that this design requires careful pulse shaping (Fig. 18a, 18b) to be able to initiate the implosion at high initial laser-driven pressure, with the sample very close to the melt curve.

Shocks can pre-process solid-state material, modifying its deformation characteristics. [Gr 82] To be able to isolate the effects of the shock(s), we have designed a configuration that can shocklessly compress the material. We build off the initial design of Barnes, but replace an HE driven detonation with a laser-driven shock to create the ram pressure that compresses the metal, as illustrated schematically in Fig. 19a. The laser drives a strong shock through a 2.3 mm thick CH driver foil. When the shock breaks out the back side, the plasma blowoff expands across the and decompresses. As the ejecta reach the thick Mo payload, the Mo is gently compressed (isentropically), as illustrated in Fig. 19b. By stacking 20 ns laser pulses, the flier is driven at $1\text{--}5 \times 10^{13}$ W/cm² for 120 ns.

This basic NIF-ICE (ie, isentropic compression experiment, adopting the acronym used in [As 99]) configuration offers considerable flexibility. In a 3-Mbar design shown in Fig. 20a, the flyer was driven at 10^{13} W/cm² for 170 ns in an 8 mm spot with a 4 mm gap, giving strain rates of $\sim 5 \times 10^6$ s⁻¹. This design requires a slight enhancement to the NIF laser to allow ~ 30 ns pulses, which are stacked back to back in 6 sets. The various profiles of pressure vs. time in the figure correspond to various depths into the Mo payload. By ~ 400 μ m into the sample, the compression wave has steepened into a shock. The 10-Mbar design shown in Fig. 20b (NIF experiment #3 in Fig. 26), is driven at 5×10^{13} W/cm² for 120 ns by stacking 6 sets of 20 ns beams, at characteristic strain rates of $\sim 5 \times 10^7$ s⁻¹.

By thinning the Mo payload up to 70 μ m, this design can be turned into an ICE-RT experiment, very much like Barnes conducted, only now at pressures of ~ 1 Mbar or more. In this case, face-on radiography is possible. In yet another design, the Mo was started out pre-melted, and refreezes in the isentropic compression. In the RT configuration, using face-on radiography, we will be able to infer the grain size distribution after refreeze, which is a fundamental question in the material dynamics community. We will also apply these same ICF techniques to Ta and other materials of interest.

The designs discussed so far were developed to scale the strain rates down to lower values (low $\times 10^6$ s⁻¹), and test the material dynamics in a shocked system versus a shockless system. The peak pressures possible in these designs, however, were ~ 10 Mbar. To venture much farther into the ultrahigh pressure regimes, we have designed a scaleup of our Nova solid-state RT experiment. The NIF hohlraum is shown in Fig. 21a, using a primary-secondary hohlraum design, with internal shields, and the planar package mounted on the secondary hohlraum wall. The outer cone NIF beams are used for the

drive, and enter from the top and bottom. The inner cone NIF beams, which are not suitable as drive beams in a shielded hohlraum, are reserved for backlighting. The primary diagnostics will be face-on and side-on radiography. Examples of face-on (Fig. 21b) and side-on (Fig. 21c) radiographs from our Nova work are shown on the right, as an illustration.

For our 10 Mbar Ta design, we use a scale-6 hohlraum. (These scale designations are based on a Nova scale 1 hohlraum, which is ~ 3 mm long and 1.6 mm diameter. A scale 6 means a factor of 6 larger in all dimensions.) We accelerate a 20- μm -thick Ta payload, and will use face-on radiography of the RT growth of preimposed sinusoidal ripples to infer the high pressure strength. The ablator is 19 μm of CH backed by 51 μm of $\text{C}_5\text{H}_6\text{F}_8$. Profiles in the Ta of pressure (P), temperature (T_e), melt temperature (T_m), and radiation drive temperature (T_r) versus time from the simulations are shown in Fig. 22a. Notice that the shaped drive has 6 steps, starting with a 25 eV “foot” lasting 10 ns, and incrementally increasing in steps to a peak of 160 eV. The peak pressure in the Ta remains above 10 Mbar for ~ 5 ns, which is sufficient time to make an RT measurement. The Ta stays a factor of ~ 5 below the predicted melt temperature in this design.

The drive for our 20 Mbar point design is shown in Fig. 22b. This is a 6-step radiation drive into a scale 5.2 hohlraum, giving a foot (first step) temperature of ~ 50 eV for ~ 8 ns, and a peak of 200 eV at 22 ns. The Ta stays a factor of ~ 3 below the predicted melt temperature in this 20 Mbar design (NIF experiment #4 in Fig. 26). We also have a 25 Mbar design, where the Ta is predicted to be a factor of ~ 2 below melt. These 6-step pulse shapes are required to reach the high pressures of 10-25 Mbar but keep the Ta solid. The minimum hohlraum size is set by hohlraum filling, which causes the laser deposition region to move away from the hohlraum wall. If there is large hohlraum filling, the laser deposition region can come into view of the package, becoming a potential source of preheat, from which the package could melt. For the 20 Mbar and 25 Mbar designs, a scale 5 hohlraum is the minimum size for which we have confidence in our designs.

We now turn to the physics of refreeze. By pre-melting the target, we turn our high pressure (10-Mbar), RT designs into refreeze experiments. The design given in Fig. 23a (NIF experiment #5 in Fig. 26), shows that pre-melted Ta refreezes unambiguously at 20.5 ns on the 4th shock at a pressure of ~ 5 Mbar, as the Ta is compressed. The foil then accelerates at a peak pressure > 10 Mbar, allowing a face-on radiography measurement of the RT growth and grain size distribution. The key physics uncertainties here are (1) what is the grain size distribution resulting from this rapid refreeze, and (2) what is the high pressure strength in this newly refrozen phase. We will infer the grain size by face-on radiography, as the inset in Fig. 23b from our Nova data motivates. Our simulations suggest that our face-on measurements should be sensitive to high pressure strength to an accuracy of better than a factor of 2, as shown by the sensitivity study shown in Fig. 23b.

To achieve 20 Mbar in the solid state in a planar package requires a series of 6 shocks. The laser power profile that generates these 6 steps is shown in Fig. 24a. The first step is at low power, and each succeeding step is at increasingly higher power, but shorter duration, until the peak at 360 TW is reached, which gives peak pressures in the Ta of $>$

20 Mbar. The drive can only use the outer cone beams (cone angles of 44 and 50 degrees), because the package would not be well shielded from the shallower angle beams. The peak contrast (peak of step 6 / peak of step 1) is 30:1, which is not overly stressful on the laser. Our 23 ns pulse length just fits within the NIF baseline design specs. We use a cocktail hohlraum, and assume the full 8 J/cm^2 damage threshold, allowed by the NIF specs.

The integrated laser drive energy is shown in Fig. 24b. The important point to illustrate here is that half the total available drive energy goes into generating the final 20 Mbar push. Without the full laser system operating to baseline specs, and the successful development of cocktail hohlraums, a 20 Mbar solid-state strength measurement seems difficult.

To be able to measure strength to better than a factor of 2 and to be able to deduce the inflight grain size will require high quality data. We illustrate this in Fig. 25 with two images taken on Nova. The image in Fig. 25a (4.3 keV Sc backlighter through $20 \mu\text{m}$ of Al) has a recorded signal to noise ratio of $\sim 4:1$, and is marginally of high enough quality to be able to infer the inflight grain size distribution. The image in Fig. 25b (8.9-9.0 keV Zn backlighter through $22 \mu\text{m}$ of Mo) has a recorded signal to noise ratio of $\sim 2:1$, and is not sufficient to be able to infer grain size. The Nova data used area backlighters. On NIF for our experiments, this technique will not be adequate, and we will switch to backlit pinhole "point" backlighters, which are much brighter. The consequence of this is that to obtain a full time sequence on a single shot will require 4 separate and independent packages (and therefore 4 separate backlighters) on a single hohlraum.

Based on these Nova images, we conclude that we need S/N of at least 5:1 to be able to infer inflight grain size. For a $20 \mu\text{m}$ Ta foil, using the 8.9-9.0 keV Zn backlighter, which falls just under the L edge of Ta at 9.9 keV, in the backlit-pinpoint-backlighter configuration, we will require 2 quads of backlighting per image. For a $20 \mu\text{m}$ U foil, we would have to backlight at 15 keV, and would require 4 quads of backlighting per image. (The full NIF laser is comprised of 48 quads, each of which consists of 4 beamlets. A quad is the smallest unit of lasers on NIF that can have an independent pulse shape and delay.) By mounting 4 independent foils on the hohlraum, we can do 4 simultaneous RT measurements, varying the time to obtain a full time sequence on a single shot. Shots on NIF will be a very valuable commodity, so obtaining a full time sequence on a single shot will be required to understand strength evolution. In other words, each shot on NIF will have to be a fully self-contained experiment.

We present all of our 14 NIF designs on a single plot of peak pressure versus strain rate in Fig. 26. The 20 and 25 Mbar designs at the top are at mid $\times 10^7 \text{ s}^{-1}$ strain rates, whereas the large-target, low strain rate designs at low $\times 10^6 \text{ s}^{-1}$ strain rates are at peak pressures in the low Mbar regimes. A particularly important regime is around 10 Mbar. Ta is predicted to undergo a bcc-to-fcc phase transition above this pressure, and the deformation mechanism (at low temperature) might change from thermal activation to phonon drag. By having designs that cover a range of more than a factor of 10 in strain rate at $P \geq 10 \text{ Mbar}$, we should be able to assess the deformation mechanism by

observing the dependence of strength with strain rate and temperature. Based on these design studies, and data taken on Nova and Omega, we conclude that to access the highest pressures shown, $P > 20$ Mbar, and make meaningful measurements will require the full NIF laser system operating to the baseline specs, and a full diagnostic suite.

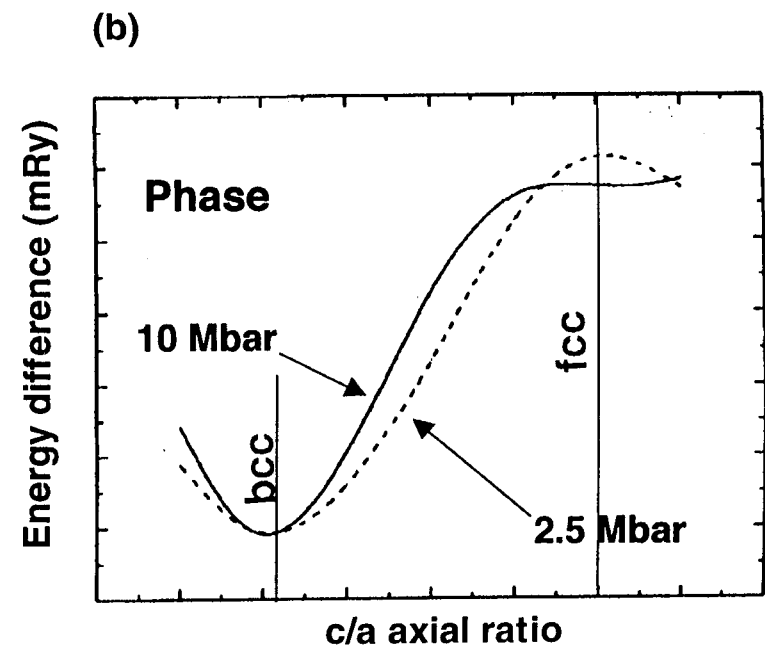
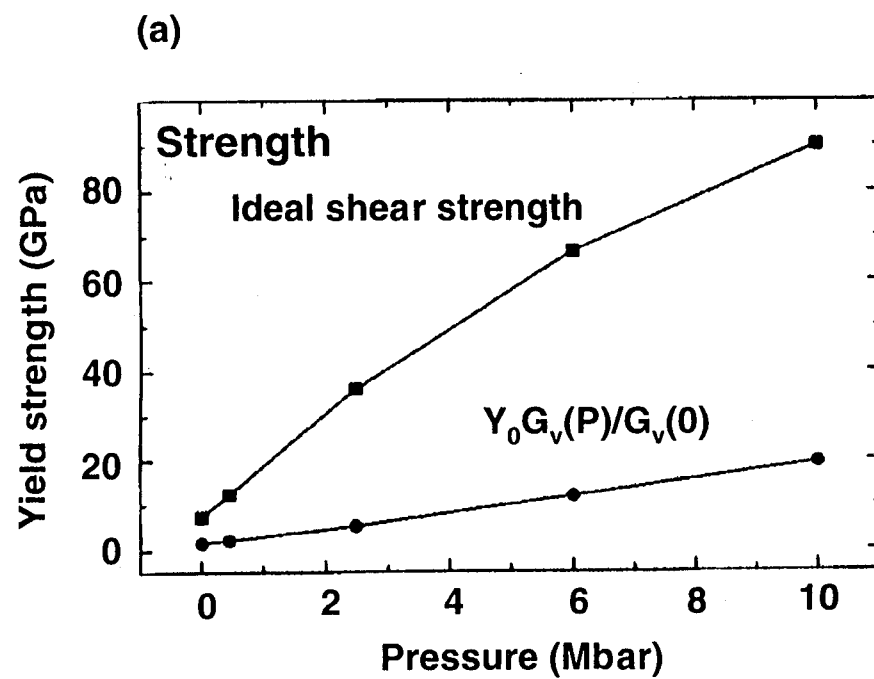
We reiterate in closing, however, that no single facility can address all of the important physics issues at all parameter regimes of interest. Rather, a coordinated plan involving multiple laboratories and universities and multiple facilities will be needed. This report presents our plan for the NIF component of this effort. We have started the initial discussions with the technical teams at LANL and SNLA to form such a coordinated effort. ICE experiments on Z, for example, will offer a valuable cross check on experiments conducted at $P < 10$ Mbar and strain rates in the mid 10^6 s^{-1} range. Atlas will offer a chance to push the strain rate scaling down another order of magnitude to the mid 10^5 s^{-1} range, albeit at lower pressures. Strain rate scaling and its effect on deformation mechanisms is probably the most important physics question to settle with experiments.

We are very grateful for many illuminating discussions with John Moriarty, Dave Lassila, John Klepeis, James Stolken, Brian Wirth, Roger Minich, Pat Egan, B. Goodwin, C. Verdon, W. Hsing, J. Kilkenny, Rusty Gray, Marc Meyers, and Jim Asay. We are also indebted to the many scientists whose results I have reproduced in this report.

References

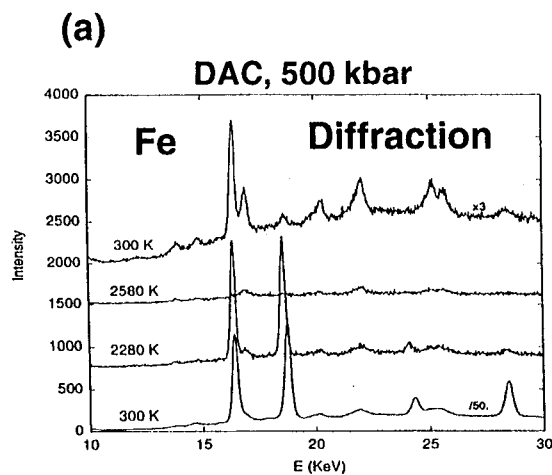
- [Al 00] d'Almeida & Gupta, Phys. Rev. Lett. **85**, 330 (2000).
- [Gr 82] D. Grady and J. Asay, J. App. Phys. **53**, 7350 (1982).
- [As 99] J.R. Asay, Shock Compression of Condensed Matter-1999, AIP Conference Proceedings CP505, ed. M.D. Furnish, L.C. Chhabildas and R.S. Hixson, pg. 261 (2000).
- [Ba 74] Barnes et al., J. Appl. Phys. **45**, 727 (1974).
- [Bu 99] K.S. Budil, private communication (1999)
- [Ch 98] E. Chandler, private communication (1998).
- [Co 01] J. Colvin et al., in preparation for submittal to Phys. Rev. Lett. (2001).
- [Gl 00] S.G. Glendinning et al., Phys. Plasmas **7**, 2033 (May, 2000).
- [Ho 77] Hoge & Mukherjee, J. Mat. Science **12**, 1666 (1977).
- [Hu 84] D. Hull and D.J. Bacon, *Introduction to Dislocations* (Butterworth Heinemann, Woburn, MA, 1984), Fig. 3.4, pg. 50.
- [Ka 00] D.H. Kalantar et al., Phys. Plasmas **7**, 1999 (2000).
- [Ka 99] D.H. Kalantar et al., Rev. Sci. Instrum. **70**, 629 (1999).
- [Kane 01] J. Kane et al., Phys. Rev. E, Rapid Commun., in press (2001)]
- [La 99] This figure originally appeared in the Lassila SI LDRD proposal.
Our addition has been to add the experimental images along the bottom.
- [Le 93] Lebedev et al., 4th IWPCTM, 81 (1993).
- [Le 96] Lebedev et al., 5th IWPCTM, 231 (1996).
- [Le 97] Lebedev et al., 6th IWPCTM, 307 (1997).
- [Lo 01] Loveridge-Smith et al., Phys. Rev. Lett., in press (2001).
- [Me 94] Marc A. Meyers, *Dynamic Behavior of Materials*,

- (John Wiley & Sones, New York 1994), Fig. 13.21, pg. 361.
- [Me 01] M.A. Meyers et al., in preparation (2001).
 - [Re 01] B.A. Remington et al., in preparation for submittal to Rev. Mod. Physics (2001).
 - [So 98] Soderlind and Moriarty, Phys. Rev. B **57**, 10340 (1998).
 - [St 81] Steinberg and Guinan, J. App. Phys. (1981)
 - [St 89] Steinberg & Lund, J. Appl. Phys. **65**, 1528 (1989).
 - [Sw 89] J.W. Swegle and A.C. Robinson, J. Appl. Phys. **66**, 2838 (1989).
 - [Wa 87] Wark et al., Phys. Rev. B **35**, 9391 (1987).
 - [Wa 89] Wark et al., Phys. Rev. B **40**, 5705 (1989).
 - [Wa 94] Wark et al., Laser Part. Beams **12**, 507 (1994).
 - [Wh 95] Whitlock and Wark, Phys. Rev. B **52**, 8 (1995).
 - [Wo 90] Woolsey et al., J. App. Cryst. **23**, 441 (1990).
 - [Wo 97] Wark et al., J. App. Phys. **81** 3023 (1997).
 - [Yo 95] C.-S. Yoo, Science **270**, 1473 (1995).

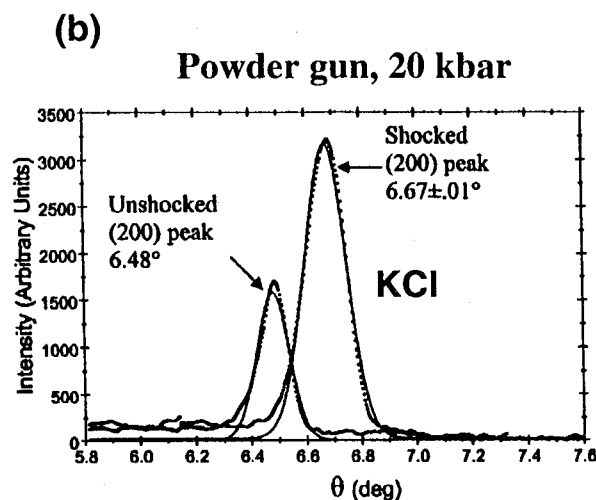


Soderlind & Moriarty, *Phys. Rev. B* 57 p. 10340 (1998)

Figure 1



Yoo, *Science* **270**, p. 1473 (1995)



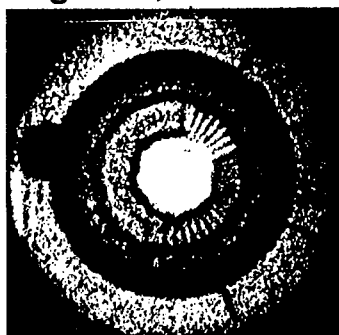
d'Almeida & Gupta, PRL **85**, 330 (2000)

(c) HE-driven plate, $P \sim 100$ kbar



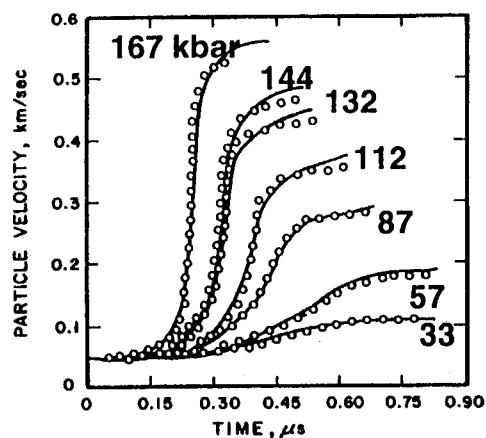
Barnes, et al., *J. Appl. Phys.* **45**, 727 (1974)

(d) Pegasus, $P \sim 100$ kbar



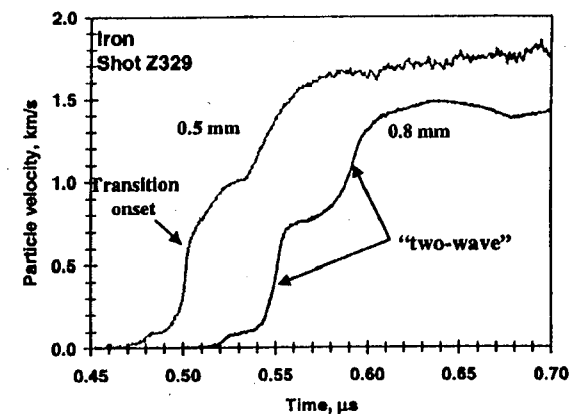
Chandler & Egan (2000)

(e) Gas-gun wave profile at ~ 100 kbar



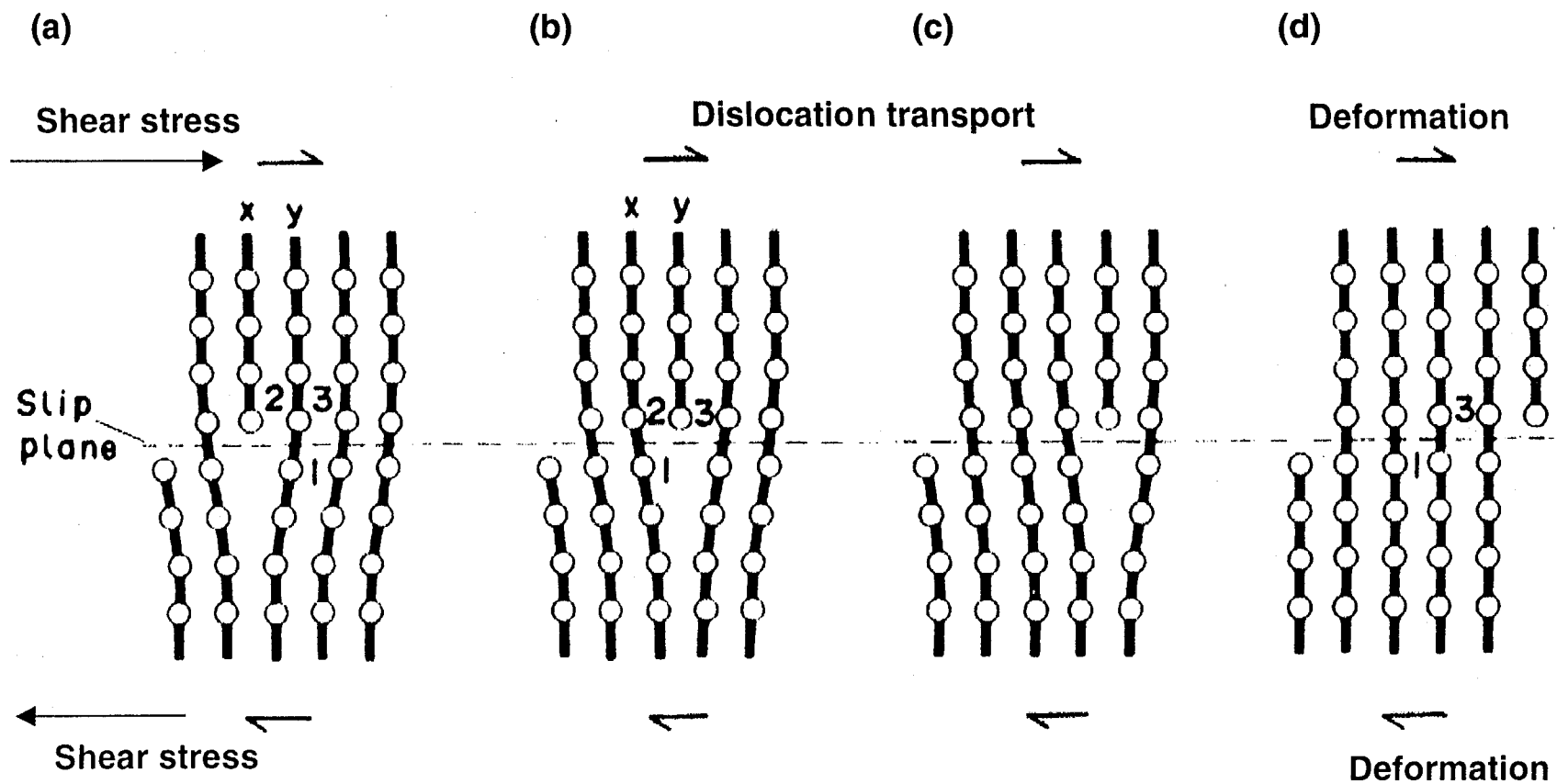
Swegle & Grady (1985)

(f) Z-ICE at 300 kbar



Asay, *Shock Compression of Condensed Matter* -1999

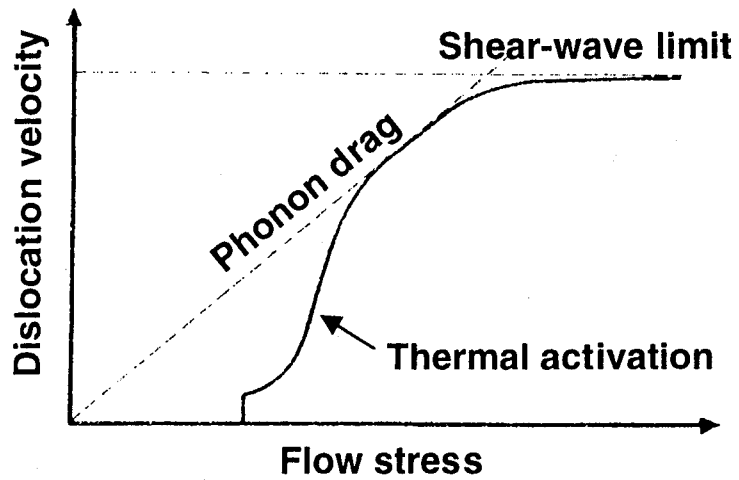
Figure 2



Hull & Bacon, *Introduction to Dislocations* (1984)

Figure 3

(a)



Meyers, *Dynamic Behavior of Materials*, pp. 358–361 (Wiley, 1994)

(b)

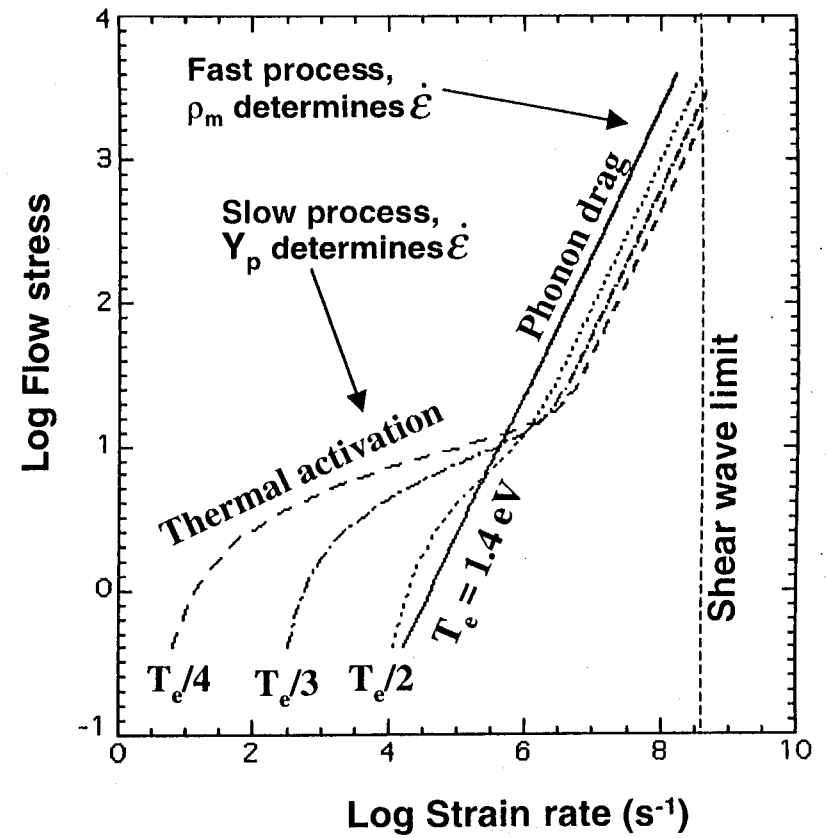


Figure 4

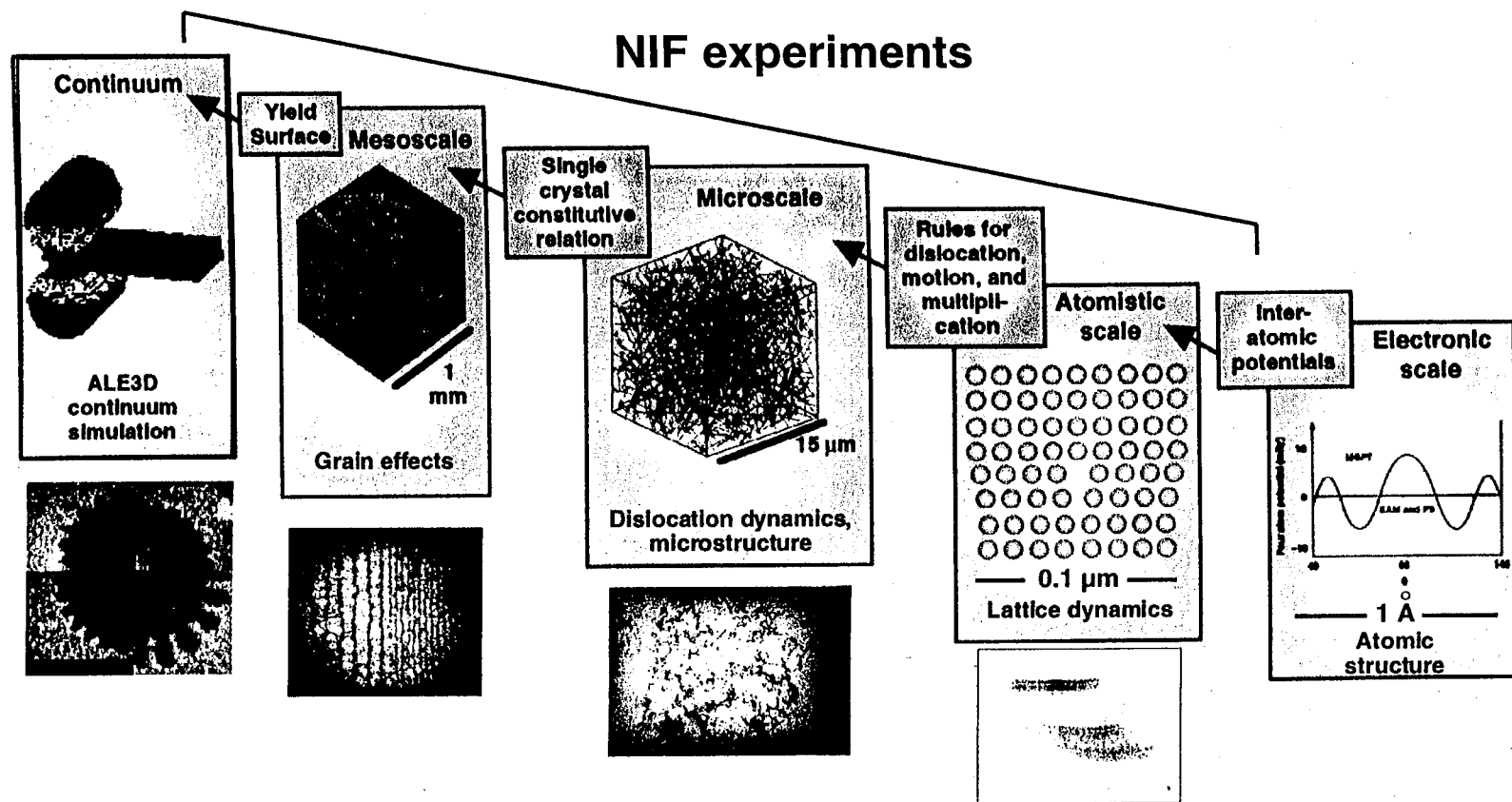
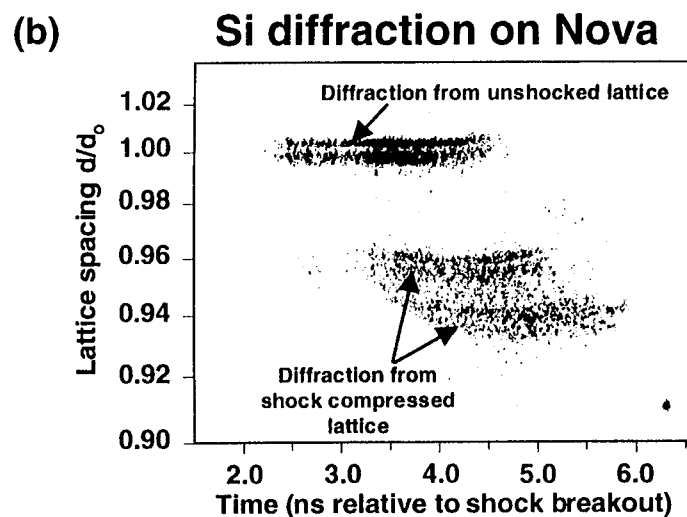
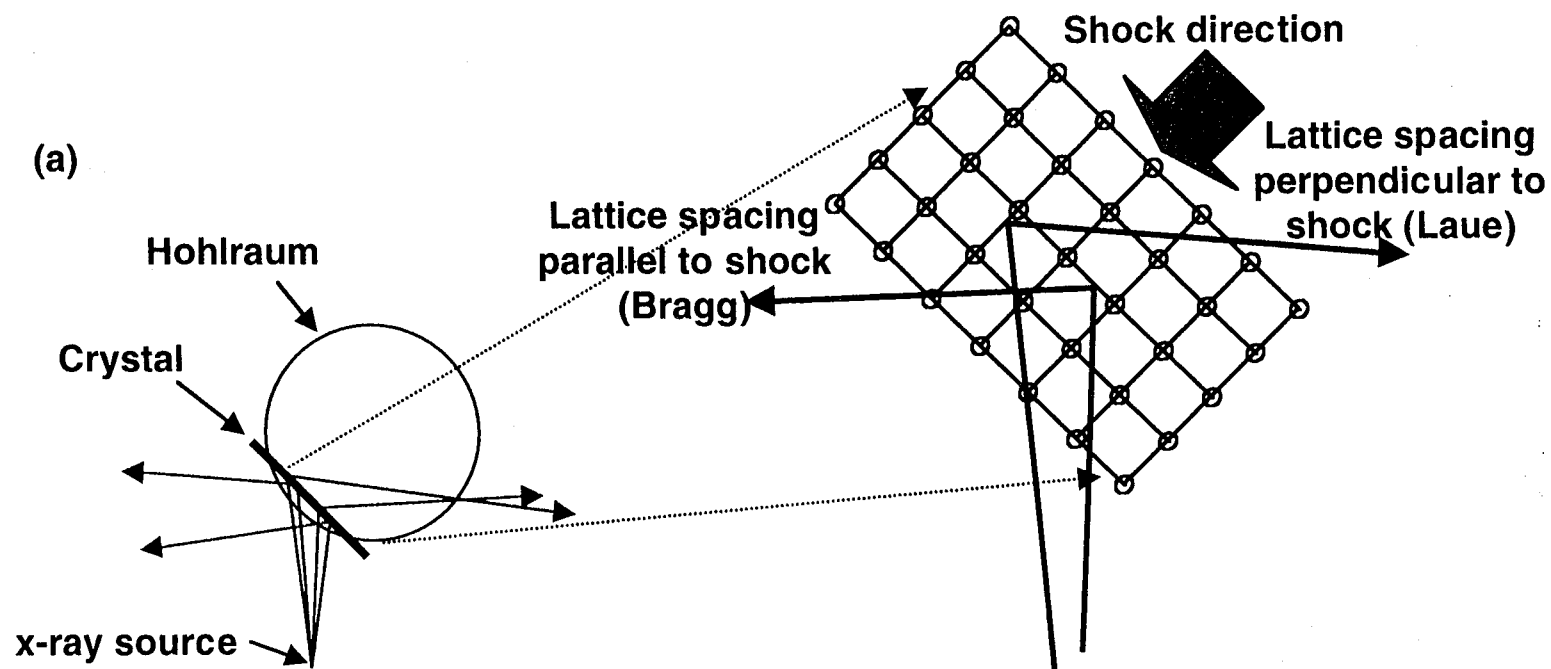
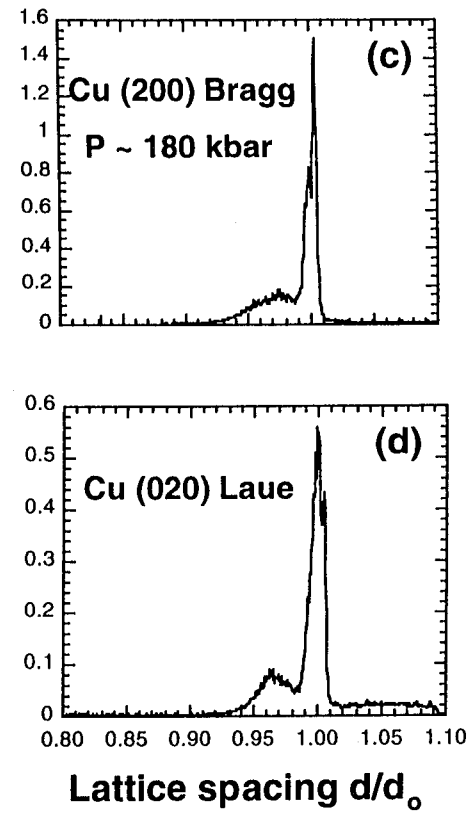
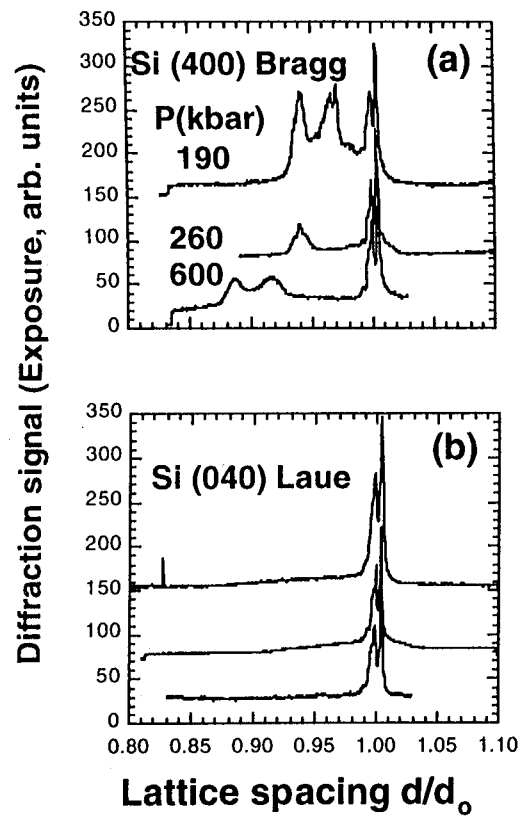


Figure 5



Kalantar, et al., *Phys. Plasmas* (5/2000)

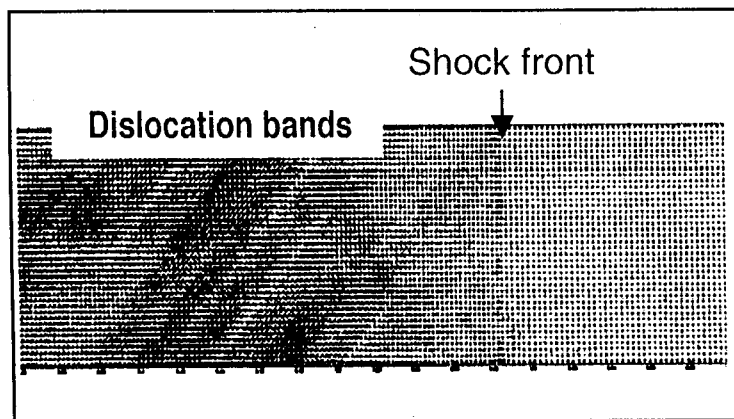
Figure 6



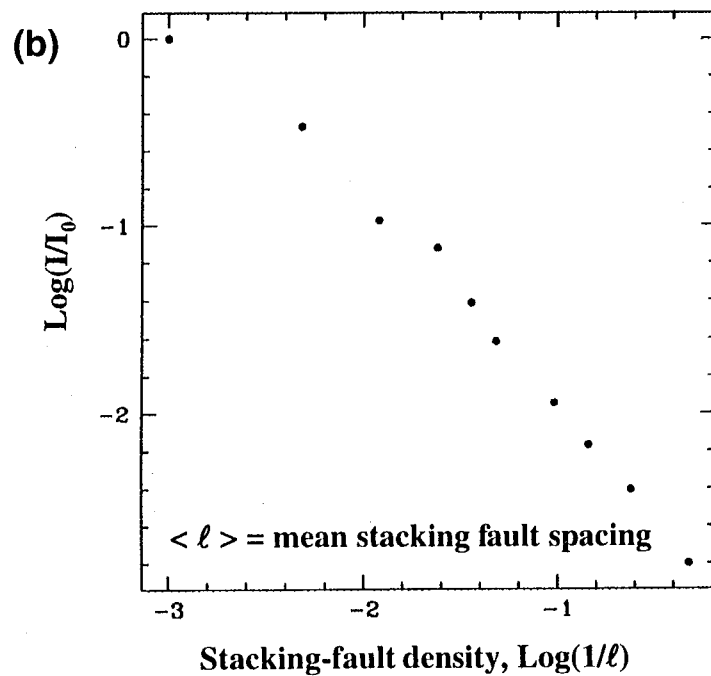
Loveridge-Smith *et al.*, *Phys. Rev. Lett.* (in press)

Figure 7

(a) MD simulation of shocked Cu

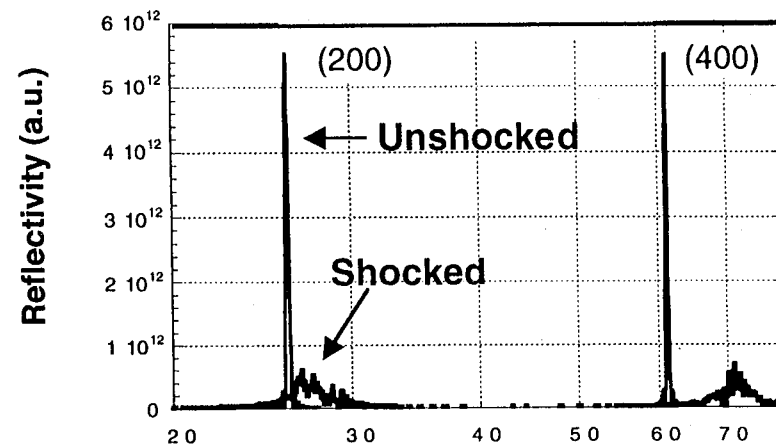


J.F. Belak (2000)



J.F. Belak (2001)

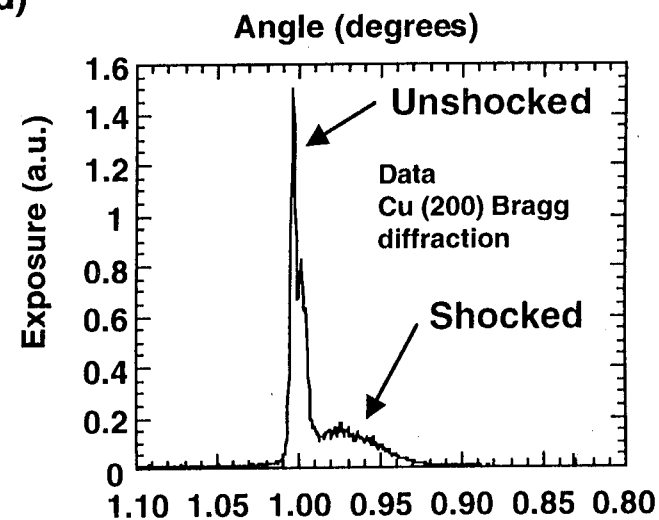
(c) Post-processed MD simulation



B. Holian & P. Lomdahl (2000)

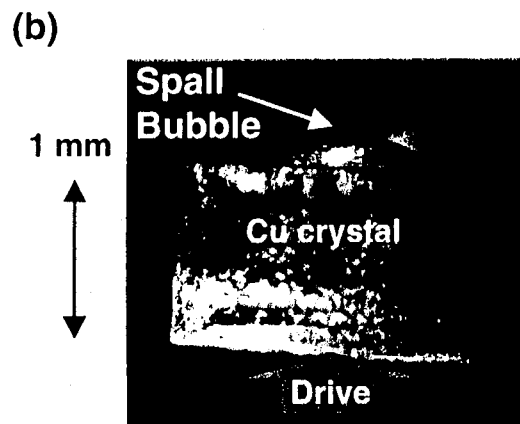
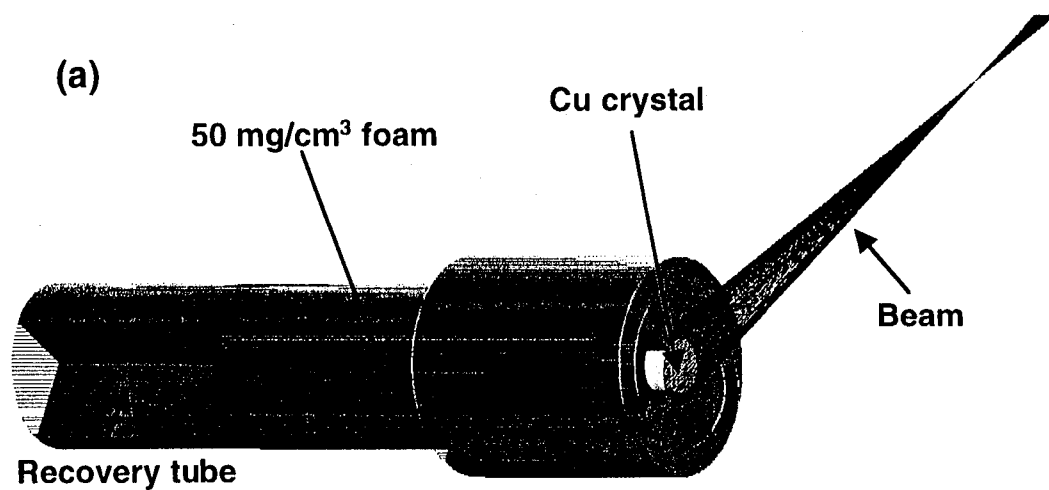
A. Loveridge-Smith and J. Wark (2000)

(d)

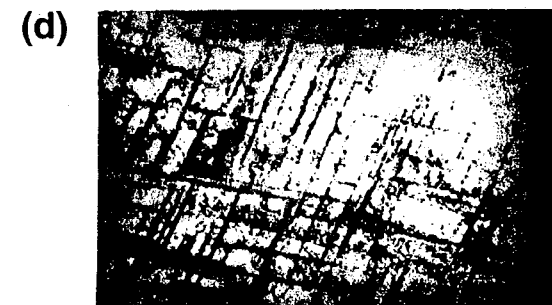


Loveridge-Smith *et al. Phys. Rev. Lett.* (in press)

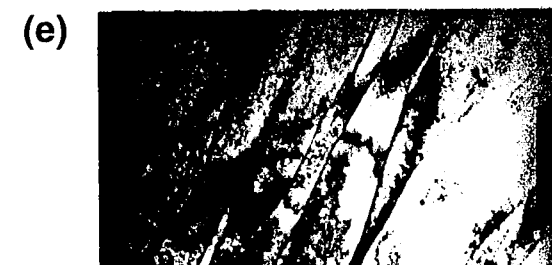
Figure 8



$E_{\text{laser}} = 40 \text{ J}$, $P \sim O(100 \text{ kbar})$



$E_{\text{laser}} = 205 \text{ J}$, $P \sim O(300 \text{ kbar})$

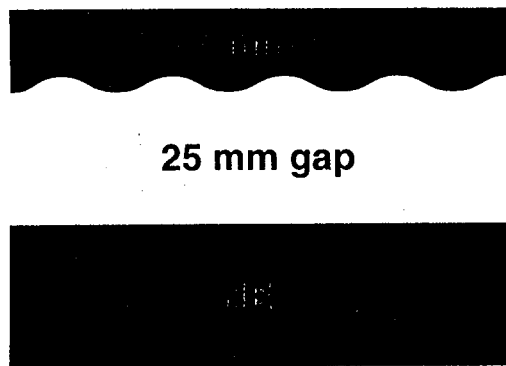


$E_{\text{laser}} = 320 \text{ J}$, $P > O(600 \text{ kbar})$

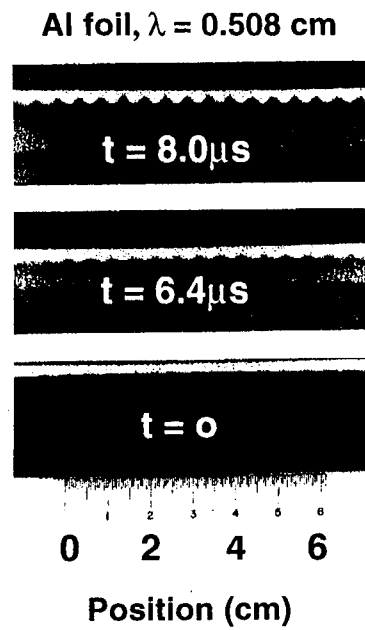
Meyers, *et al.*, in preparation, (2001)

Figure 9

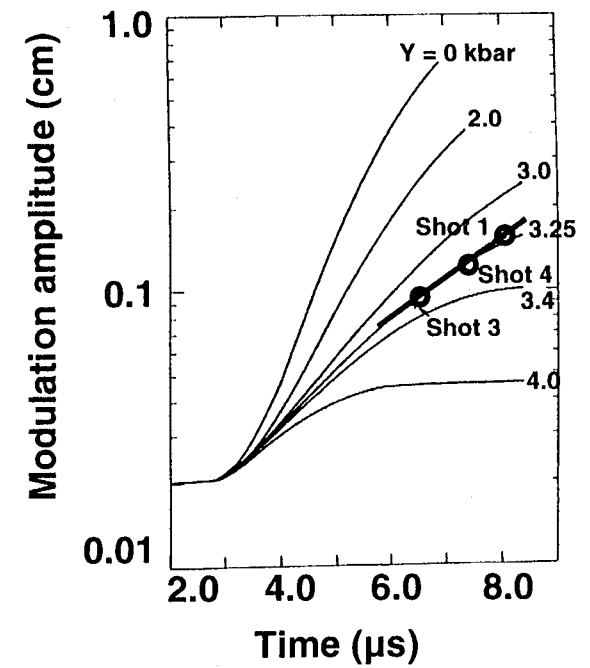
(a)



(b)

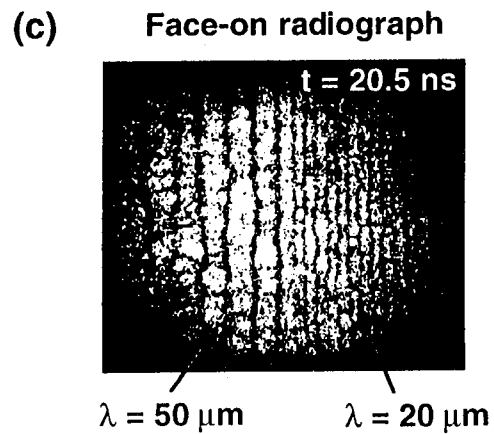
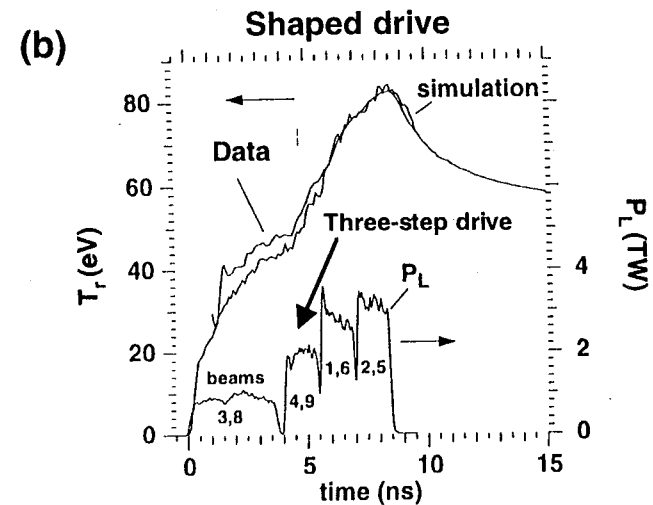
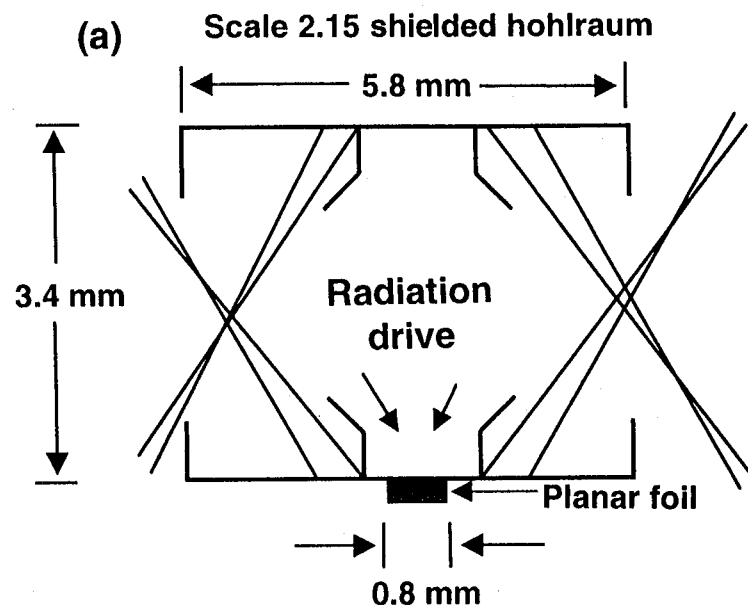


(c)



Barnes, et al., *J. Appl. Phys.* 45, 727 (1974)

Figure 10



Kalantar *et al.*, *Phys. Plasmas* (5/2000)

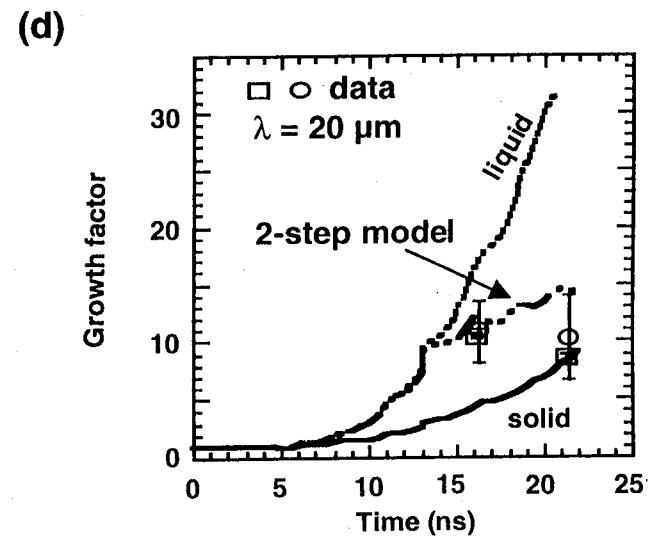
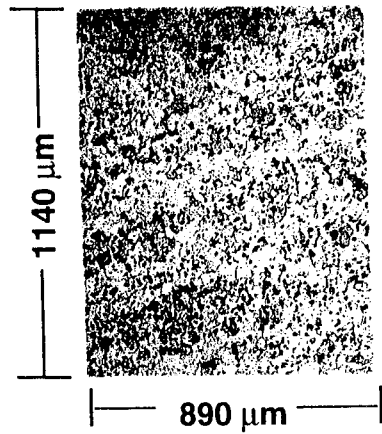


Figure 11

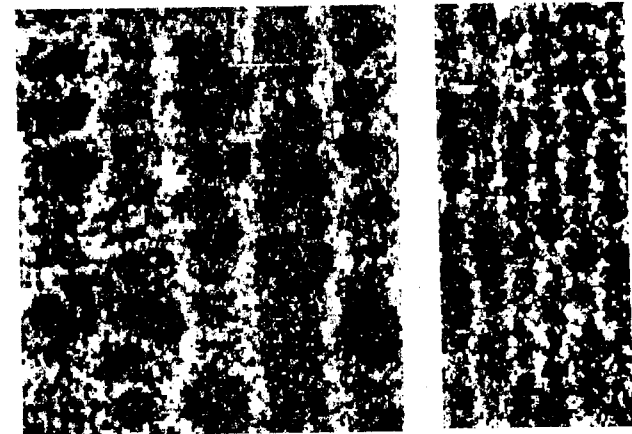
(a)

Initial grain characterization, 6061 Al



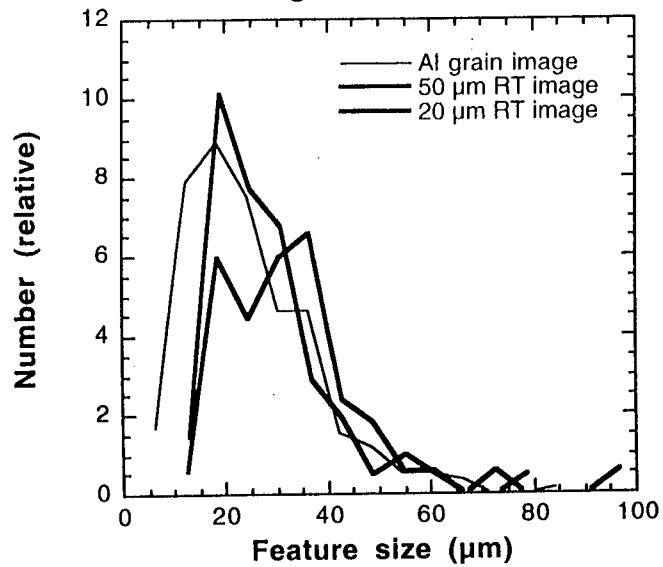
(b)

Nova data, $t = 20.5 \text{ ns}$



(d)

Deduced grain size distribution



(c)

Grain analysis

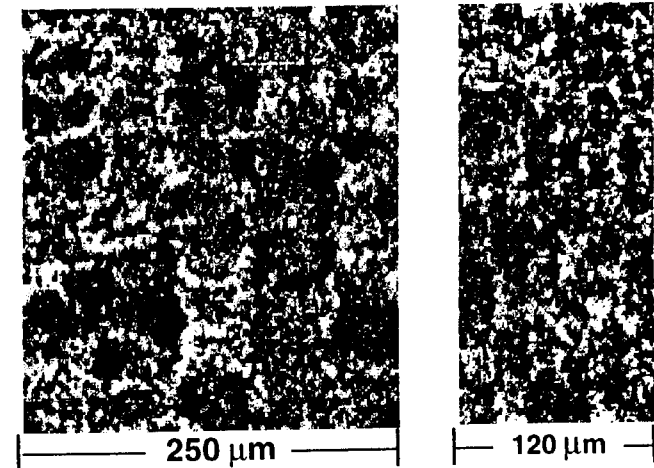
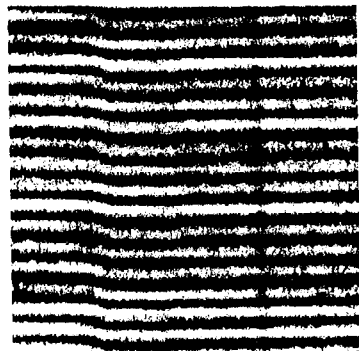
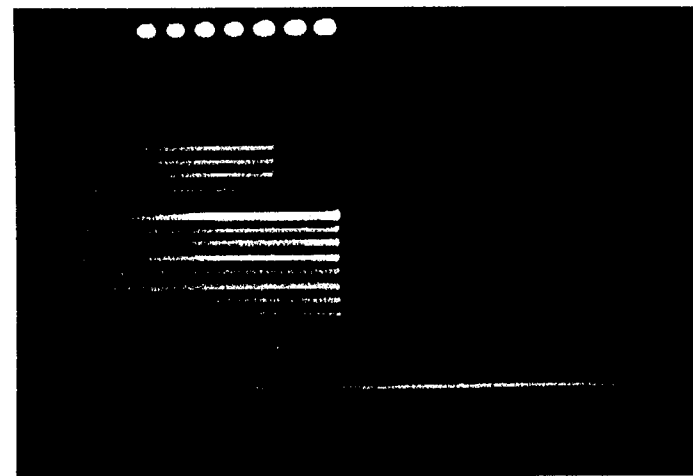


Figure 12

(a) Shock profile VISAR data on
200 μm Al backed by LiF



(c) Shock timing data using
a stepped CH (Br) foil



(b) Resulting Al shock wave profile

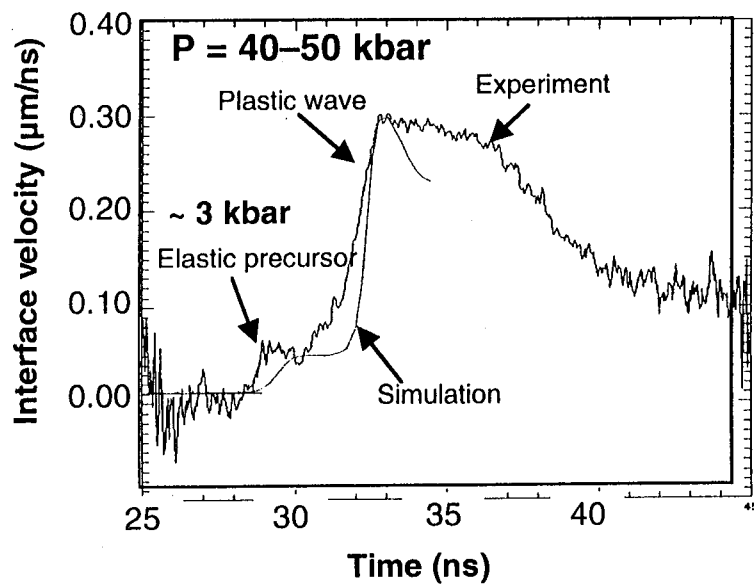
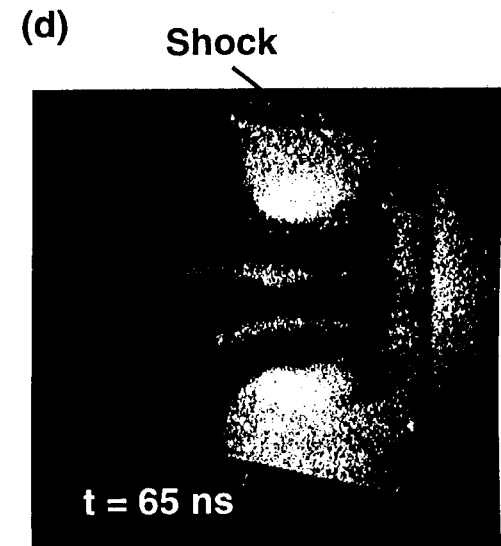
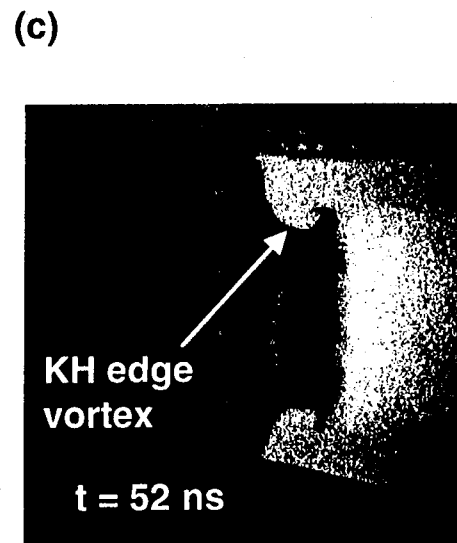
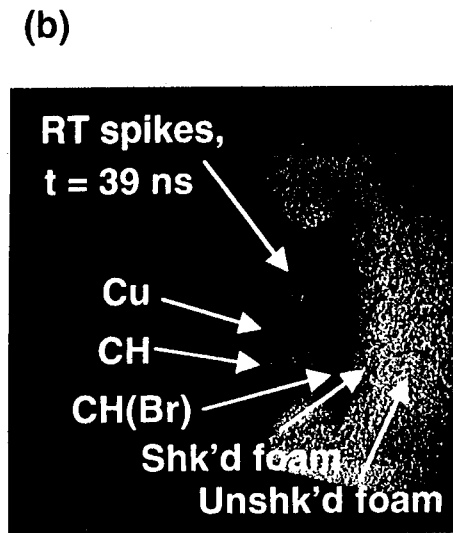
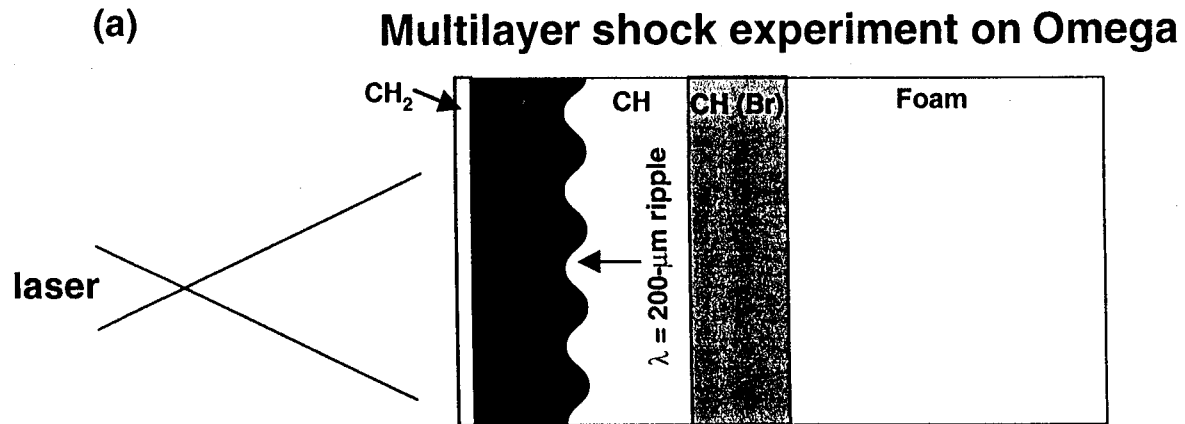


Figure 13

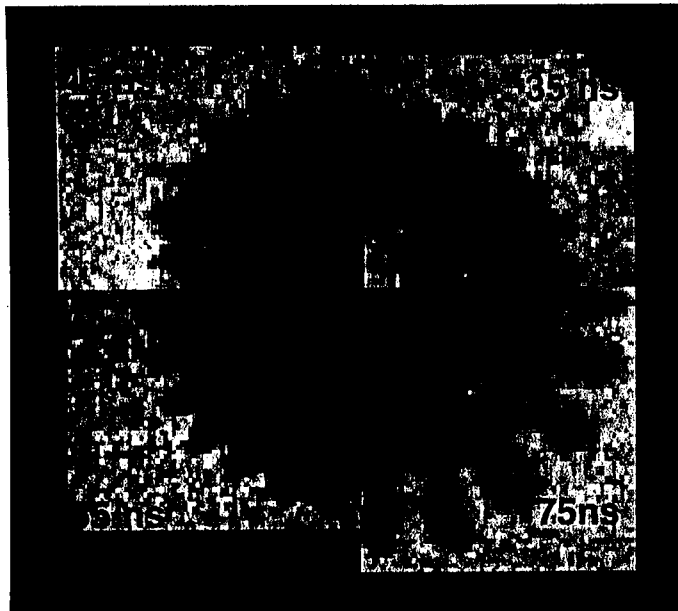


Kane and Robey, *Phys. Rev. E* (in press, 2001)

Figure 14

(a)

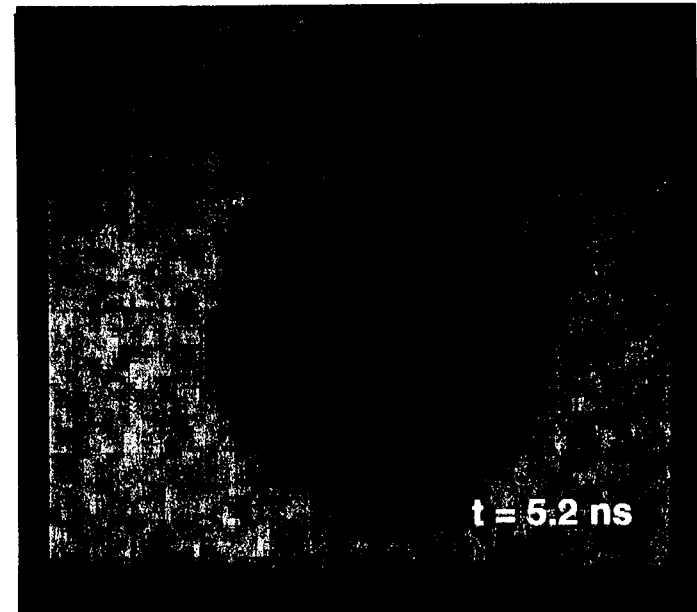
Cylindrical explosion on Nova



Budil (1999)

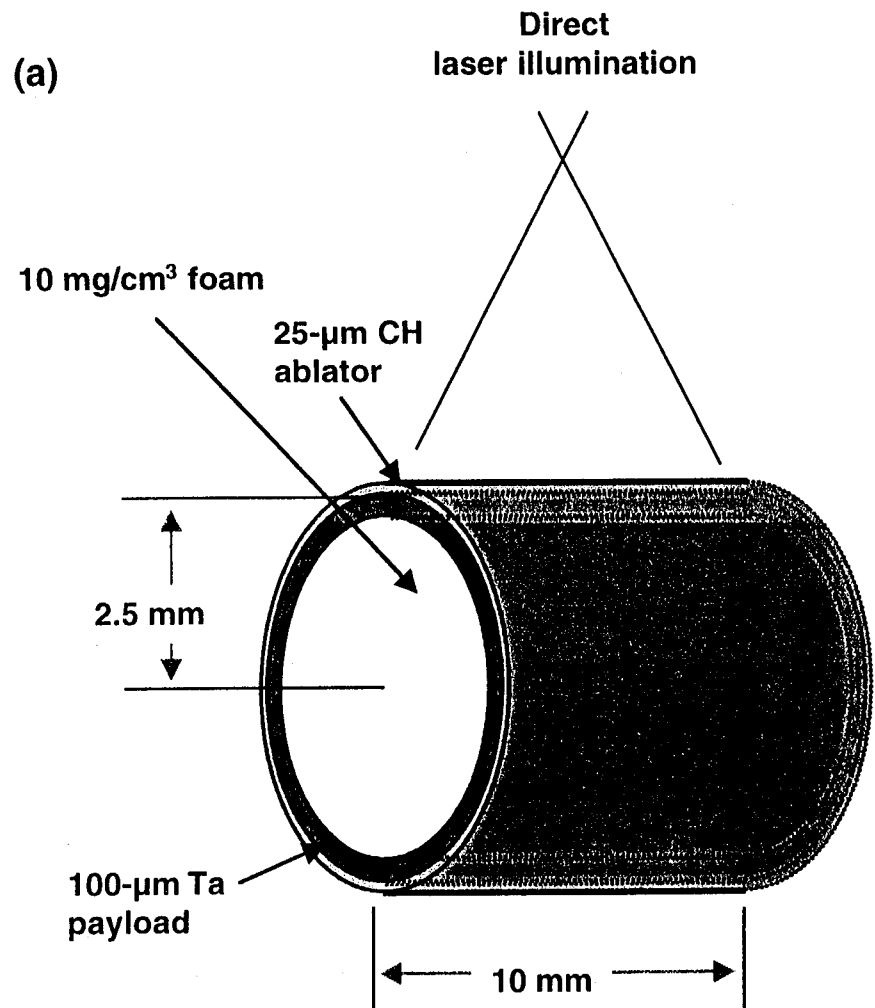
(b)

Spherical implosion on Nova



Glendinning, *et al.*, *Phys. Plasmas* (5/2000)

Figure 15



(b)

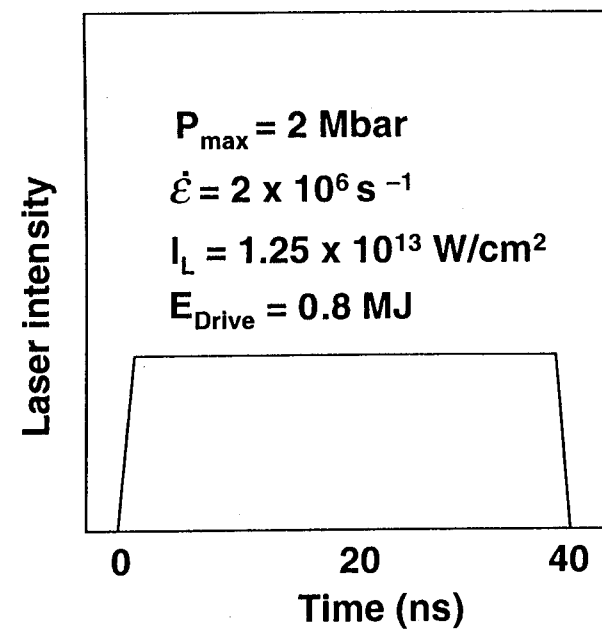


Figure 16

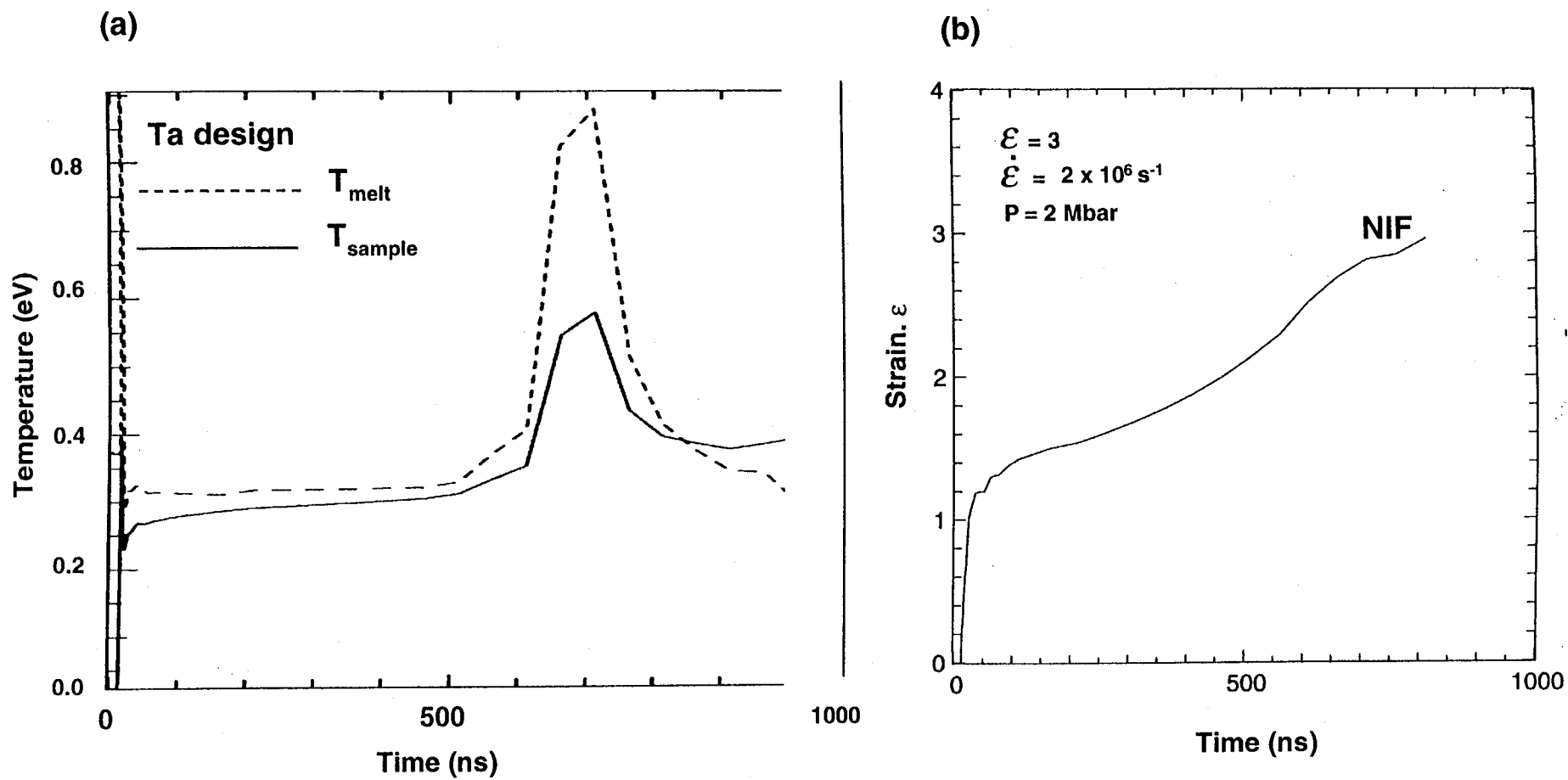
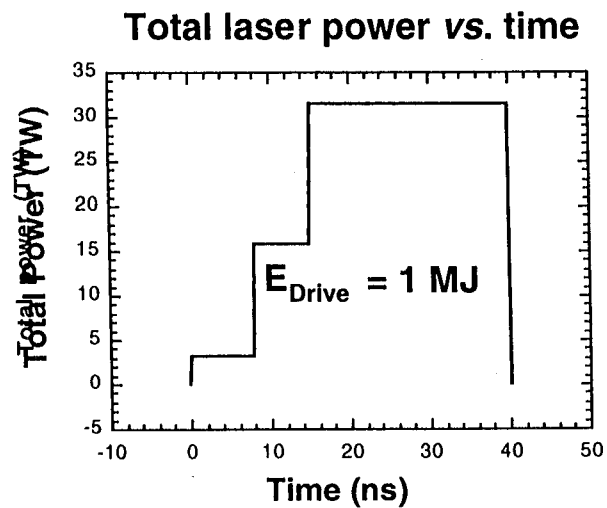
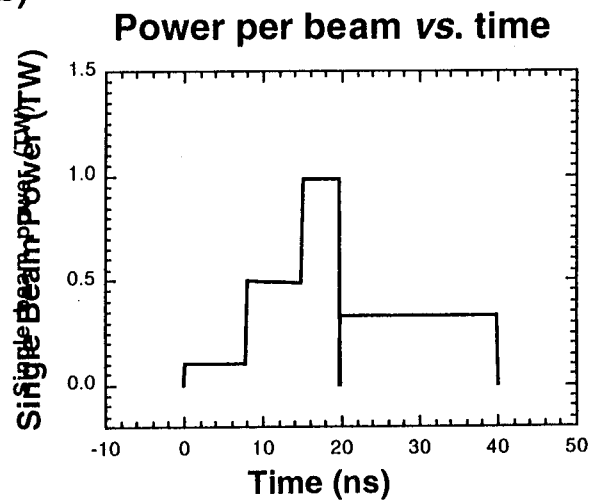


Figure 17

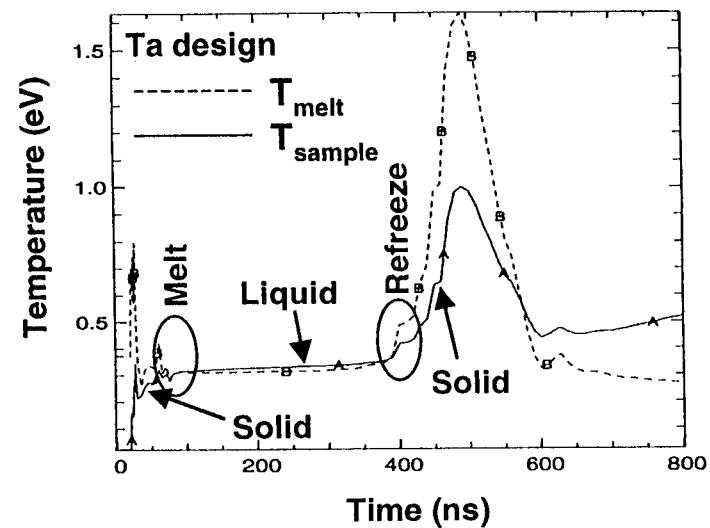
(a)



(b)



(c)



(d)

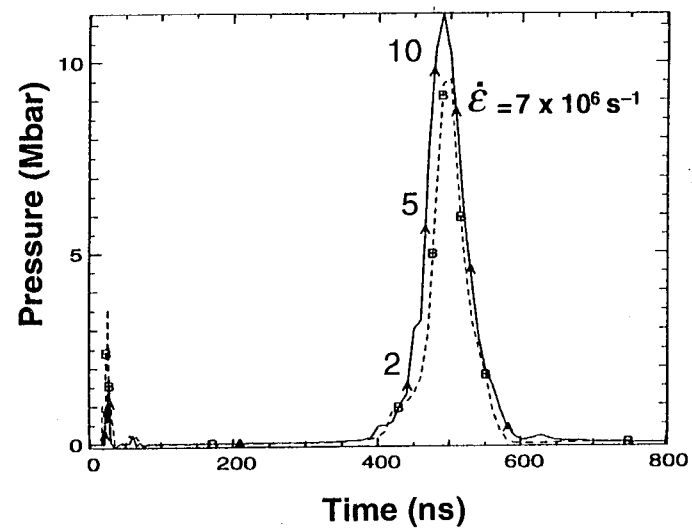
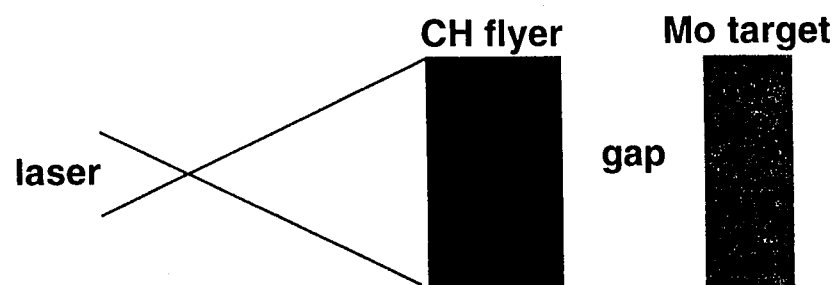


Figure 18

(a)

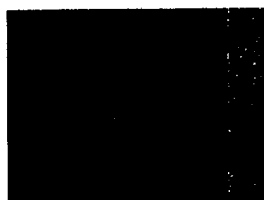
1. Launch driver foil blowoff with a shock



2. Blowoff expands towards target



3. Blowoff gently compresses target (isentropically)



(b)

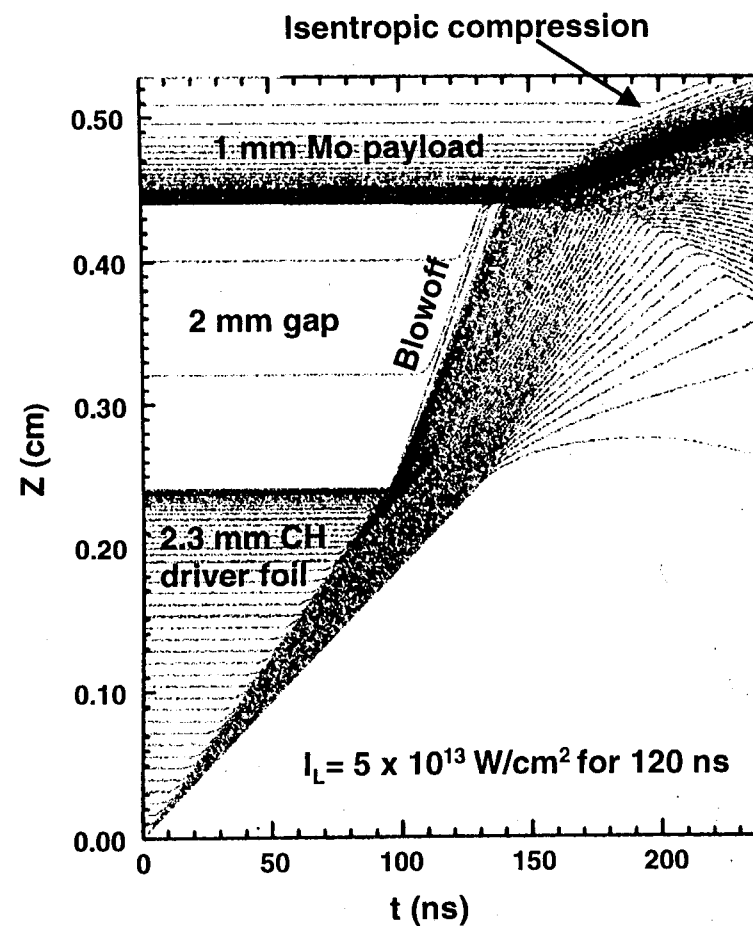
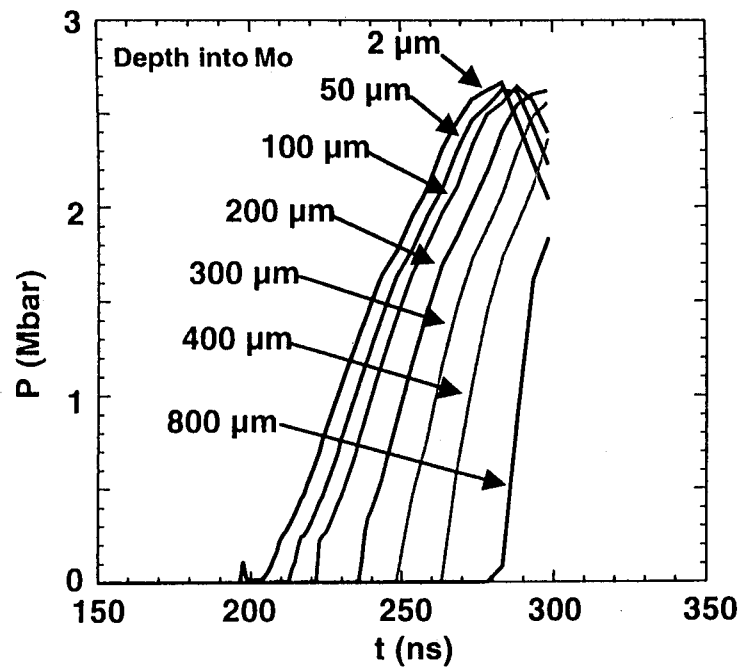


Figure 19

(a)

3-Mbar Mo design



(b)

10-Mbar Mo design

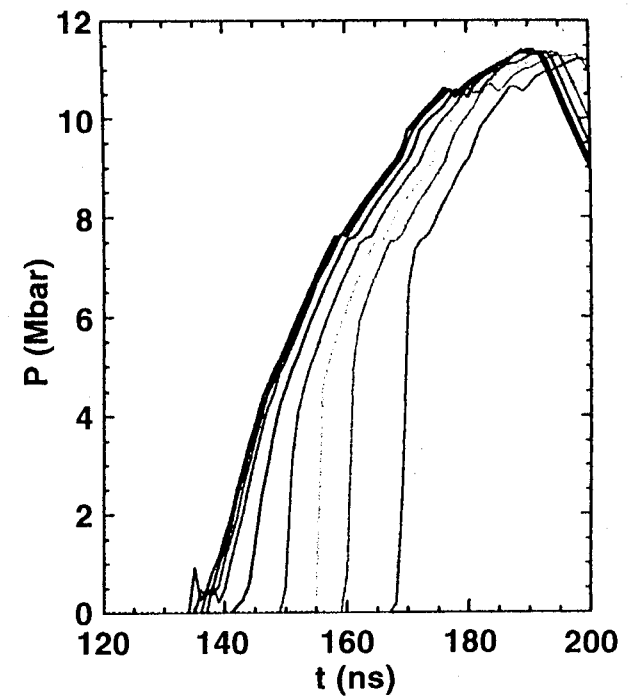
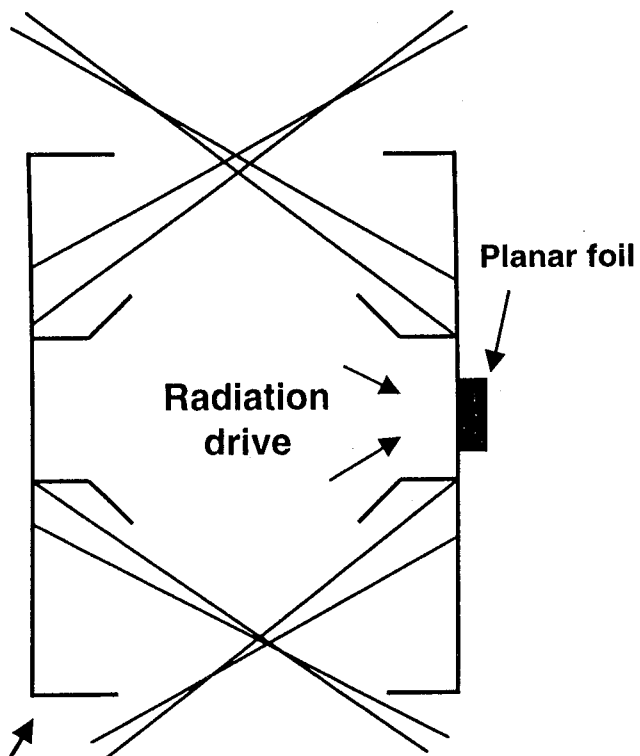


Figure 20

(a)

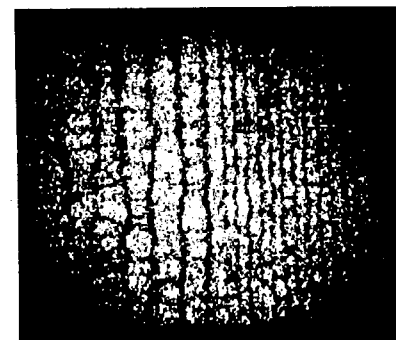
NIF hohlraum



Scale 5.2 shielded hohlraum

(b)

Nova Al experiment,
 $P = 0.2\text{--}1.2$ Mbar,
Face-on image,
 $\lambda = 50, 20\text{ }\mu\text{m}$,
 $t = 20.5\text{ ns}$



(c)

Side-on image from a Cu experiment

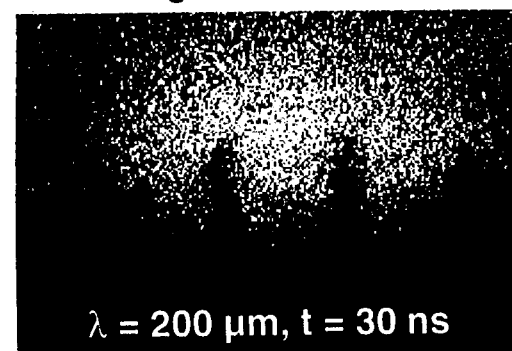


Figure 21

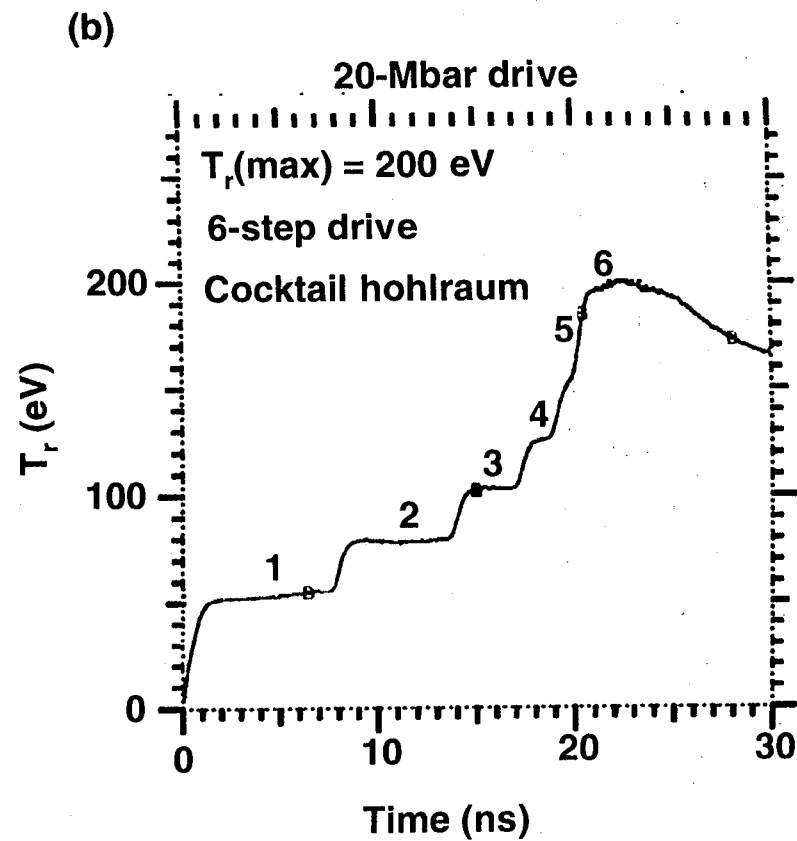
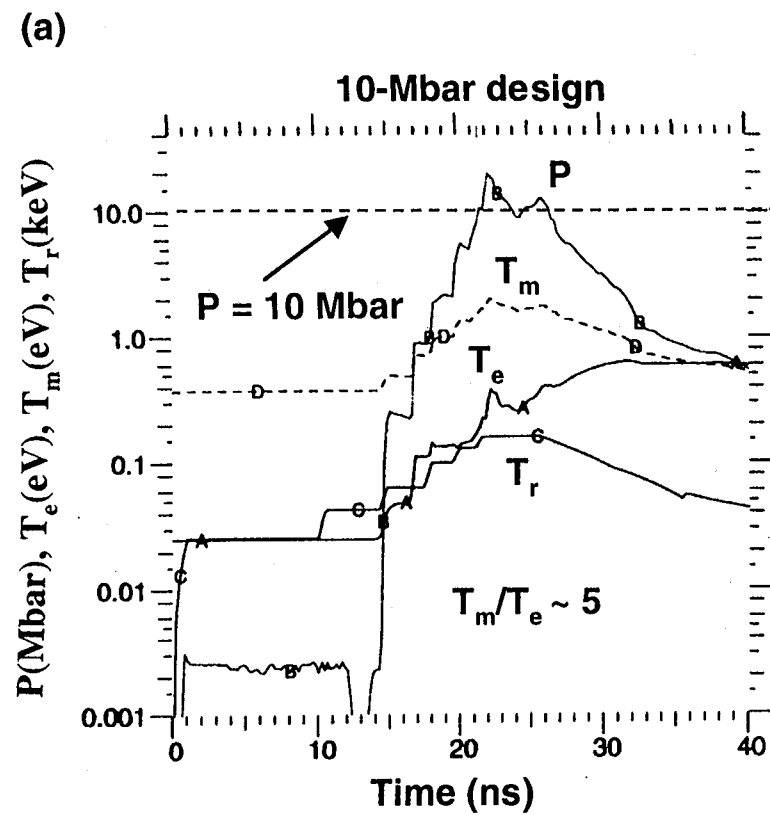
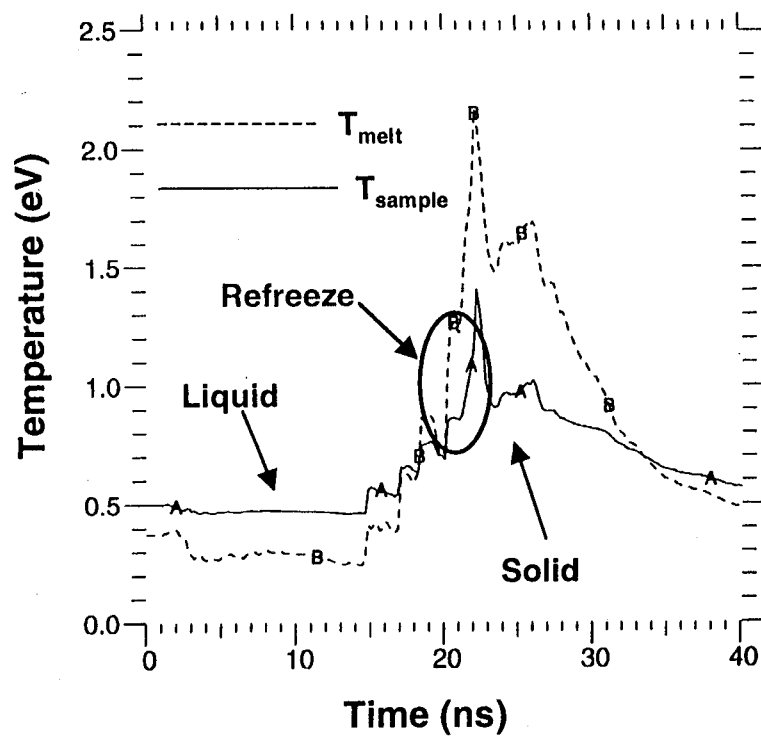


Figure 22

(a)



(b)

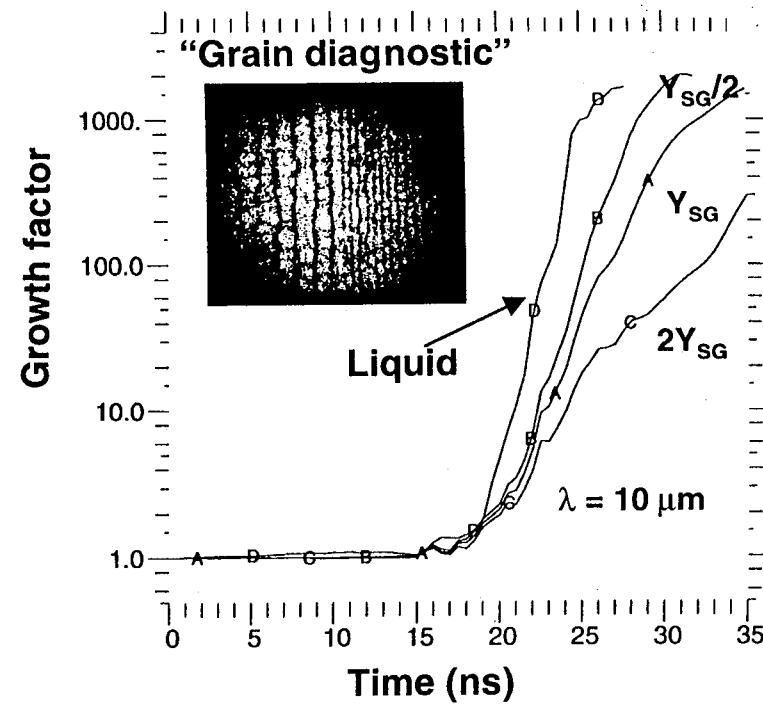
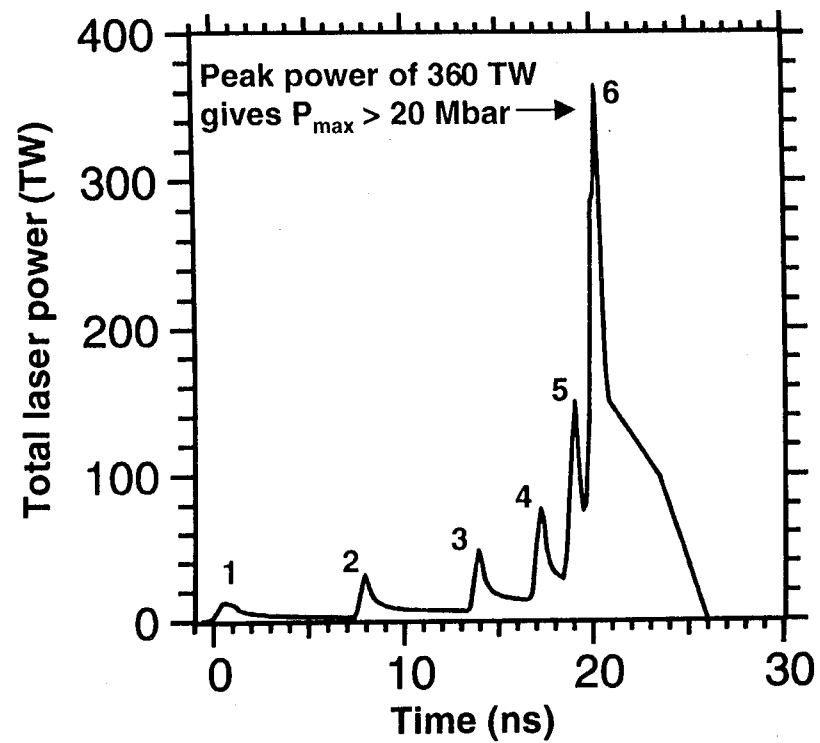


Figure 23

(a)



(b)

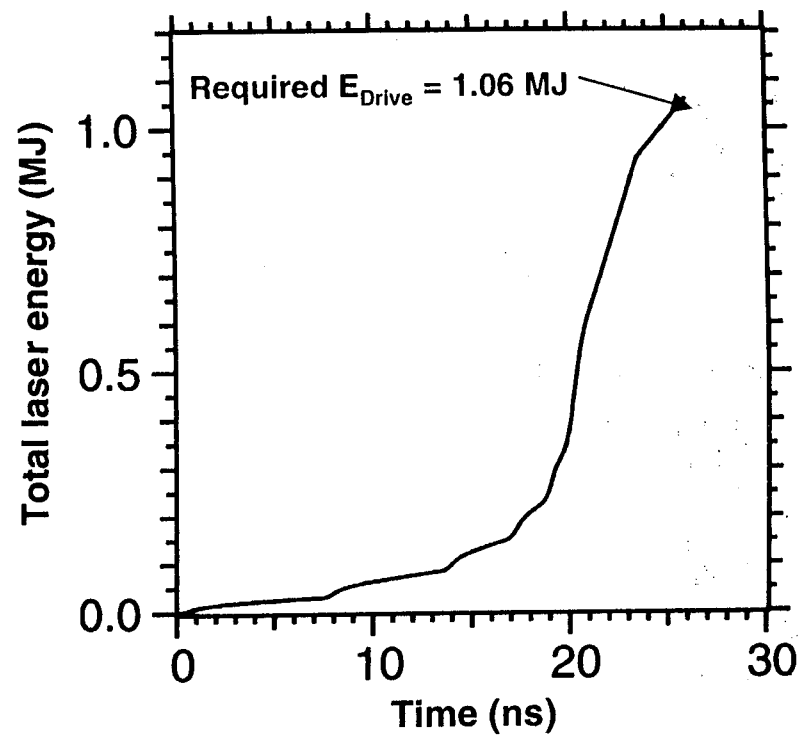
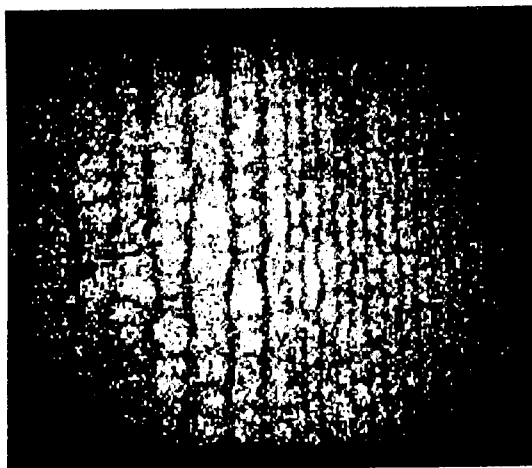


Figure 24

(a)

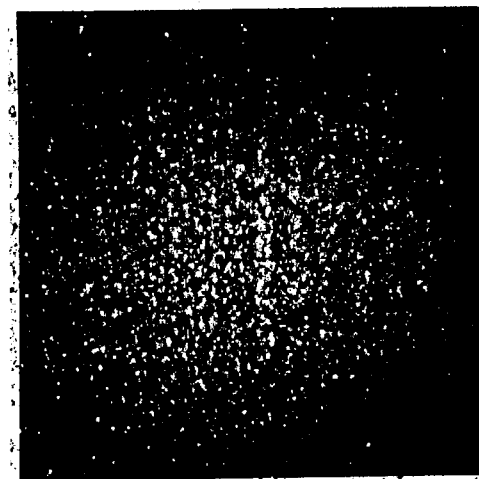
20- μ m Al at 4.3 keV on Nova



Marginally acceptable

(b)

20- μ m Mo at 9 keV on Nova



Unacceptable

Figure 25

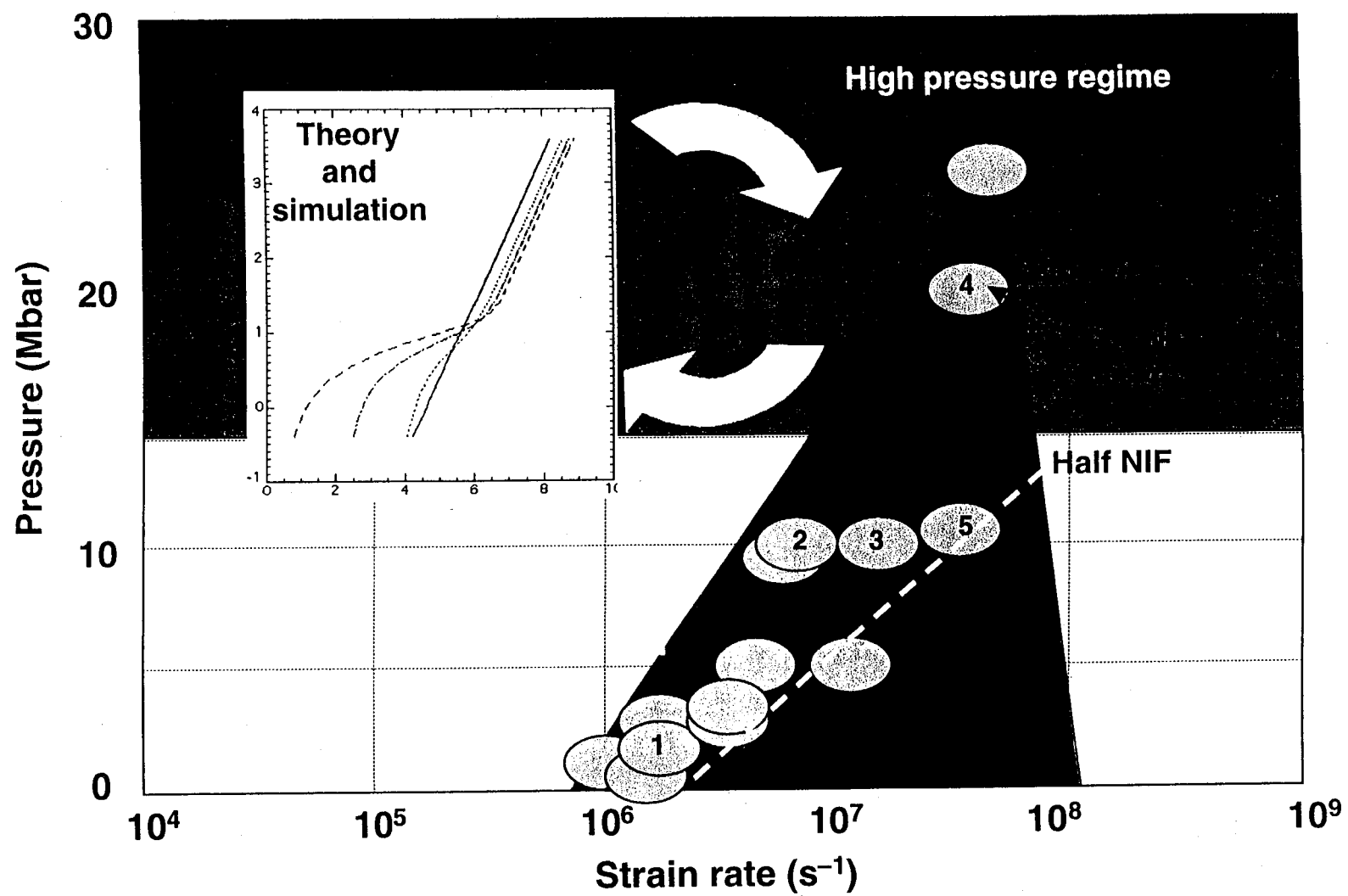


Figure 26

University of California
Lawrence Livermore National Laboratory
Technical Information Department
Livermore, CA 94551